Available online at www.sciencedirect.com
ScienceDirect
Mathematics and Computers in Simulation 203 (2023) 609–632
MATHEMATICS AND COMPUTERS IN SIMULATION
www.elsevier.com/locate/matcom

Original Articles

Spatio temporal dynamics of direct current in treated anisotropic tumors

Antonio Rafael Selva Castañeda[a,b], Josue Mariño del Pozo[b], Erick Eduardo Ramirez-Torres[c], Eduardo José Roca Oria[b], Sorangel Bolaños Vaillant[d], Juan I. Montijano[a,*], Luis Enrique Bergues Cabrales[e,*]

[a] *Instituto Universitario de Investigación de Matemáticas y Aplicaciones, Universidad de Zaragoza, Zaragoza, Spain*
[b] *Departamento de Telecomunicaciones, Facultad de Ingeniería en Telecomunicaciones, Informática y Biomédica, Universidad de Oriente, Santiago de Cuba, Cuba*
[c] *Departamento de Ingeniería Biomédica, Facultad de Ingeniería en Telecomunicaciones, Informática y Biomédica, Universidad de Oriente, Santiago de Cuba, Cuba*
[d] *Servicio de Imagenología, Hospital Provincial Docente Saturnino Lora Torres, Santiago de Cuba, Cuba*
[e] *Dirección de Ciencia e Innovación Tecnológica, Centro Nacional de Electromagnetismo Aplicado, Universidad de Oriente, Santiago de Cuba, Cuba*

Received 22 October 2021; received in revised form 30 May 2022; accepted 5 July 2022
Available online 11 July 2022

Abstract

The inclusion of a diffusion term in the modified Gompertz equation (Cabrales et al., 2018) allows to describe the spatiotemporal growth of direct current treated tumors. The aim of this study is to extend the previous model to the case of anisotropic tumors, simulating the spatiotemporal behavior of direct current treated anisotropic tumors, also carrying out a theoretical analysis of the proposed model. Growths in the mass, volume and density of the solid tumors are shown for each response type after direct current application (disease progression, partial response, stationary partial response and complete remission). For this purpose, the Method of Lines and different diffusion tensors are used. The results show that the growth of the tumor treated with direct current is faster for the shorter duration of the net antitumor effect and the higher diffusion coefficient and anisotropy degree of the solid tumor. It is concluded that the greatest direct current antitumor effectiveness occurs for the highly heterogeneous, anisotropic, aggressive and hypodense malignant solid tumors.

Keywords: Modified Gompertz equation; Anisotropic and heterogeneous malignant solid tumors; Electrochemical therapy; Diffusion tensor

1. Introduction

Low-level direct current (DC) has been used to treat all types of superficial or visceral tumors, both malignant and benign [78]. It is easy to perform as well as safe, effective and inexpensive, inducing a minimum of adverse effects on the organism. It can be carried out on an out-patient basis and applicable to tumors when oncoespecific (e.g., surgery, chemotherapy, and radiotherapy) and biological (e.g., immunotherapy) therapies fail. Furthermore, DC

* Corresponding authors.
E-mail addresses: monti@unizar.es (J.I. Montijano), berguesc@yahoo.com (L.E.B. Cabrales).

https://doi.org/10.1016/j.matcom.2022.07.004

may be best suitable for cancers near critical organs where surgery and/or radiation therapy have failed or could not be performed without damaging other normal parts. This physical magnitude not only reduces costs of chemotherapy, radiotherapy, hyperthermia, electroporation and immunotherapy, but also improves compliance. Additionally, DC may be suitable for nonresectable tumors and can save functional tissues [13,40,42,46,48,78]. Unlike radiotherapy, electrochemical treatment actives the immune system [39,40] and inhibits metastasis [81]. These results are generally reported for a single DC stimulus of duration 30–60 min (preclinical studies) [13,31,33,39,40,42,46,48] or 1–3 h (clinical studies) [42,78].

Pupo et al. [58] summarize the different DC antitumor mechanisms reported in the literature, such as: electrochemical; immune system stimulation; both electrochemical reactions (fundamentally those in which reactive oxygen species are involved) and immune system stimulation; lost of tissue water for electro-osmosis; change in the membrane potential of tumor cells; increased expression of dihydronicotinamide adenine dinucleotide phosphate dehydrogenase (NADPH) oxidase subunits-derived reactive oxygen species which subsequently induces apoptosis. Despite this diversity of DC antitumor mechanisms, the most accepted is the electrochemical one [8,29,36,39,46,48,58]. This latter may be argued because the tumor areas around the positive electrode (anode) becomes highly acidic due to the attraction of negatively charged chloride ions and the formation of hydrochloric acid (pH $<$ 3) when DC is applied to the tumor. The tumor areas around the negative electrode (cathode) become highly basic (pH $>$ 10) due to the attraction of positively charged sodium ions and the formation of sodium hydroxide. In addition, chlorine gas and hydrogen gas emerge from the entry points of the anodes and cathodes, respectively [58]. These changes in pH lead to depolarization of cancer cell membranes and cause tumors to be gently destroyed. Furthermore, the DC application causes electrolysis, electrophoresis, electro-osmosis and electroporation that lead to both microenvironmental chemical and micro-electrical field changes [8,36,39,48,58,78]. Other biochemical alterations around the anode and cathode in DC treated tumors are the following: acid hemoglobin around the anode, tissue hydration, hydrogen ions (from water electrolysis), and oxygen and chlorine gas emissions. Meanwhile, in the cathode, they report tissue dehydration, hydroxyl ions, (from water electrolysis), and hydrogen gas emissions. Water concentration and pH do not change halfway through the pair of electrodes and the areas away from them when tumors are treated with DC [48,58].

On the other hand, the death of several mice bearing the F3II mammary carcinoma (highly invasive and metastatic tumor) is observed during and after DC application [31,33]. Furthermore, DC therapy is not recognized as an oncoespecific therapy because its action mechanism is poorly understood and an electrode array has not been established yet [7,8,31,33,59]. Although, temporary changes of mass and volume in untreated and DC treated tumors are frequently reported in the literature [13,31,40,42,48,78], changes in space–time density are less commonly found [5]. From the experimental point of view, knowledge of these aspects requires a significant amount of time, animal handling and financial resources. Therefore, the use of mathematical modeling is preferred. A survey on mathematical models applied to problems in oncology and further references can be found in [47].

The DC intensity applied to the tumor is introduced in the Gompertz conventional equation, named modified Gompertz equation (MGE), to describe different types of tumor responses after DC application, such as: disease progression (DP), stable disease (SD), partial response (PR), stationary partial response (SPR) and complete remission (CR) [4]. Cabrales et al. [4] report that these five types of tumor responses depend on (i/i_0) ratio, where i is DC intensity applied to the tumor and i_0 the induced in the tumor due to DC action. CR and SPR are obtained for i/i_0 values greater than $(i/i_0)_{th}$, where $(i/i_0)_{th}$ is a threshold value of i/i_0. It is important to notice that the conventional Gompertz equation is a particular case of MGE when DC intensity is equal to zero. Subsequently, Cabrales et al. [5] introduce the diffusion term MGE, named MGE-d, to know how the mass, volume and density of spherical and isotropic solid tumors change for DP, SD, PR and CR. These four antitumor responses are reported when electrochemical therapy [31,33,42,48,78] and other types of anti-cancer therapies [50] are used.

Although the spherical tumor model is used in different experimental [63,79] and theoretical [5,59] studies, the cancer generally adopts a non-spherical geometry during its growth with prevalence of intra-tumor heterogeneity and anisotropy [9,14,21,30,31,33]. Intra-tumor heterogeneity is due to the fact that different cancer cells may show distinct morphological and phenotypic profiles (cellular morphology, gene expression, metabolism, motility, proliferation and metastasis). Intra-tumor heterogeneity, tumor anisotropy (due to space-dependent blood perfusion) and large inhomogeneous vascularization have essential roles for the progression and metastasis of cancer, ineffectiveness of the immune system and the resistance to anti-cancer therapies [10,16,49].

The tumor density has been associated to the highest probability of cancer risk [20], the limited penetration of antitumor drugs in solid tumors [35], correlation with early tumor responses [76], regulation of matrix metallo

proteinases to enhance cancer cell migration [44], among others [53]. In addition, diffusion-weighted magnetic resonance imaging allows differentiating the intra-tumor density, anisotropy and heterogeneity between the tumor and the surrounding normal tissue [18]. That is why, the diffusion tensor should be included in the mathematical approach developed in [5], as in other experimental [17,28] and theoretical [38,43,56,61,70] studies.

Despite the unquestionable scientific advances mentioned above, we are not aware of how the space–time maps of the solid tumor density and its temporal behaviors of mass and volume change with the degree of anisotropy and the type of tumor response after application of DC. Therefore, the aim of this study is to simulate the MGE-d to know how the mass, volume and density of the DC treated tumor change with its degree of anisotropy as well as the post-treatment tumor response type.

First, in Section 2 we propose the mathematical model that includes a diffusion tensor to reproduce the anisotropic growth of the tumor, and we analyze it theoretically, giving conditions on the parameters of the model to guarantee the boundedness of the tumor. In Section 3, we show some simulations and in Section 4, we give a discussion. Finally, we give some conclusions.

2. Materials and methods

2.1. Mathematical model

Cabrales et al. [5] propose the MGE-d (Eq. (1)) for the isotropic and spherical solid tumors:

$$\frac{dv(\mathbf{x},t)}{dt} = \alpha^* v(\mathbf{x},t) - \beta v(\mathbf{x},t) ln\left|\frac{v(\mathbf{x},t)}{v_{ob}(\mathbf{x})}\right| + v(\mathbf{x},t)\frac{(\alpha^*)'}{\beta}\left(1-e^{-\beta t}\right) + \nu \Delta_{\mathbf{x}} v(\mathbf{x},t), \tag{1}$$

with

$$\alpha^* = \left[a_1\left(1-e^{-\gamma t}\right)+a_2\right]\alpha, \tag{2}$$

$$(\alpha^*)' = \alpha\gamma a_1 e^{-\gamma t}, \tag{3}$$

$$a_1 = \left(\frac{i}{i_0}\right)\left(2-\frac{i}{i_0}\right), \tag{4}$$

and

$$a_2 = \left(1-\frac{i}{i_0}\right), \tag{5}$$

where, the variable $\mathbf{x}$ represents each point (x, y, z) inside the tumor and t the time (in days). $v(\mathbf{x}, t)$ is the tumor density at the point $\mathbf{x}$ at time t and $v_{ob}(\mathbf{x})$ is a reference density related to the maximum capacity of growth as suggested in [9]. $v(\mathbf{x}, t)$ and $v_{ob}(\mathbf{x})$ are given in g/mm^3. $dv(\mathbf{x}, t)/dt$ $(in$ g/mm^3 days) is the first derivate of $v(\mathbf{x}, t)$ respect t. The parameter ν (in mm$^2/days$) is the diffusion coefficient, which is independent of $\mathbf{x}$ for anisotropic tumor. $\Delta_{\mathbf{x}} v(\mathbf{x}, t)$, is the Laplacian of $v(\mathbf{x}, t)$ respect $\mathbf{x}$. The parameters α and α^* are the rates of tumor growth before and after DC application, respectively. Both parameters are given in days^{-1}. The parameter $(\alpha^*)'$ (in days^{-2}) is the first derivate of α^* with respect to time. The parameter β (in days^{-1}) is the tumor deceleration factor associated with the anti-angiogenesis endogenous process. The dimensionless parameters a_1 and a_2 depend merely on i/i_0 ratio, where i (in mA) is DC intensity applied to the tumor and i_0 (in mA) the induced in the tumor due to DC action. i_0 is the polarization current that appears in the tumor due to the polarization induced in it during the application of the steady electric field. Cabrales et al. [4] report that DP, SD, PR, SPR and CR depend on (i/i_0) ratio. CR and SPR are obtained for i/i_0 values greater than $(i/i_0)_{th}$, where $(i/i_0)_{th}$ is the threshold value of i/i_0 and depends on the tumor histological variety. Ciria et al. [13] and González et al. [31] report experimentally that Ehrlich, fibrosarcoma Sa-37 and F3II mammary solid tumors reach their complete responses from a certain $(i/i_0)_{th}$ value. This may be explained from the electrosensitivity of each cancer tumor histological variety. The parameter γ (in days^{-1}) is the first order exponential decay rate of the net effect induced in the solid tumor after DC is removed and its inverse is the decay constant (or decay-time) that characterizes the duration of such effect [5,13,31,33,58].

We use the gompertzian model in Eq. (1) because the Gompertz model is more feasible to fit tumor growth kinetics (TGK) than other models (e.g., the logistic model) [30,52,71]. Furthermore, DC parameters only appear

explicitly in MGE and MGE-d. These two equations uniquely describe the different responses of DC treated tumors. None of the equations reported in the literature to describe TGK contemplates these two aspects. These issues constitute the advantages of our model with regards to similar models.

The structure of Eqs. (2), (4), and (5) may be argued by the following reasons:

1. In Eq. (2), the modification to parameter α^* may be justified by the necrosis and/or apoptosis induced into the solid tumor after DC treatment.
2. If the solid tumor is not perturbed with DC ($i = 0$), then $\alpha^* = \alpha$, condition that is valid if the term inside the bracket is equal to 1, which is guaranteed for $a_1 = 0$ and $a_2 = 0$.
3. The solid tumors may be considered as real dielectrics because their values of electric permittivity and electric conductivity are different from zero [26] and in analogy to the dielectric materials, a general relation between the polarization, the electric field ($\vec{E}$) and the higher terms in $\vec{E}$ may be established [45].
4. The term $e^{-\gamma t}$ was also introduced to explain the solid tumor dielectric relaxation when the polarization disappears due to the removal of external electric field.
5. We believe that in dependence on the (i/i_0) ratio and the sign of parameter α^*, a DC treated tumor response is reached, which is guaranteed with Eqs. (2), (4), and (5).

The first term in the right-hand side of Eq. (1) is linked to the DC treated tumor growth, which depends on the tumor histological variety, durability of tissue damage induced in the tumor and i/i_0 ratio, as experimentally corroborated in previous studies [4,13,31,33]. The second term is responsible for the sigmoidal growth (a non-exponential growth type) of the untreated solid tumors by an overexpression of different endogenous anti-angiogenic factors (e.g., thrombospondins, angiostatin and endostatin) that inhibit pro-angiogenic factors [3,4,31,33].

Although the influence of DC on endogenous anti-angiogenic factors has not been experimentally demonstrated, the third term may represent how i/i_0 and γ parameters may promote/inhibit endogenous anti-angiogenic factors for a tumor histological variety given. This may suggest that DC may behave like an antiangiogenesis therapy (potentiate angiogenic micovascular endothelial cells) when tumor growth is inhibited and metastasis is restricted. These occurs for i/i_0 values greater than $(i/i_0)_{th}$ and lower γ values, conditions for which SPR and CR are reached [4]. By contrast, DC therapy may stimulate angiogenesis (grow of new blood vessels from pre-existing vessels) when tumor growth, progression, and metastasis are stimulated. This happens for i/i_0 values lower than $(i/i_0)_{th}$ and greater γ values. For this case, DP, SD and PR are observed [4]. This aspect may be justified from ischemia–reperfusion injury induced in solid tumors during and after DC application, as documented several researchers [41]. ischemia–reperfusion injury or reoxigenation injury is the tissue damage caused when blood supply returns to tissue after a period of ischemia or hypoxia (lack oxygen). The fourth term is introduced to represent diffusion processes that happen in solid tumors, as reported in [9,30,47,77]. Diffusion processes in cancer may be studied by means of diffusion-weighted imaging and Restriction Spectrum Imaging, which allow to estimate tumor cellularity on the basis of apparent diffusion coefficient maps. This coefficient is negatively correlated with Cellularity (cell packing density) [77].

Anisotropic tumor growth has been observed in preclinical [4,9,13,30,31,33] and clinical [42] studies. Consequently, we introduce the diffusion tensor in Eq. (1) to simulate how the mass, volume and density of the solid tumor change during and after DC treatment. Diffusion tensor has been considered in other studies [17,28,56,70].

2.2. Assumptions

1. The solid tumor is assumed as a linear, anisotropic and non-homogeneous three-dimensional medium, and it has ellipsoidal geometry with three orthogonal diameters well defined during its growth, as we observed in the experiment [4,9,13,30,31,33,42]. A schematic representation of scalene ellipsoid tumor and its three diameters (L_1, L_2 and L_3) are shown in Fig. 1. L_1, L_2 and L_3 are the tumor major diameter (along the x axis), tumor medium diameter (along the y axis) and tumor minor diameter (along the z axis), respectively. The x, y and z axes are tumor growth directions. These three diameters satisfy $L_1 \gg L_2 > L_3$, aspect verified in preclinical [9,13,21,31,33,40,48,50] and clinical [42,78] studies. Typical values of L_1, L_2 and L_3 cannot be given because they depend on the tumor histological variety and its initial size (choose by the researcher for the experiment in animals or the first volume detected by the physician in clinics. It should be noted that tumor size should not exceed 10% of body weight of animals in preclinical studies [9,21,31,33].

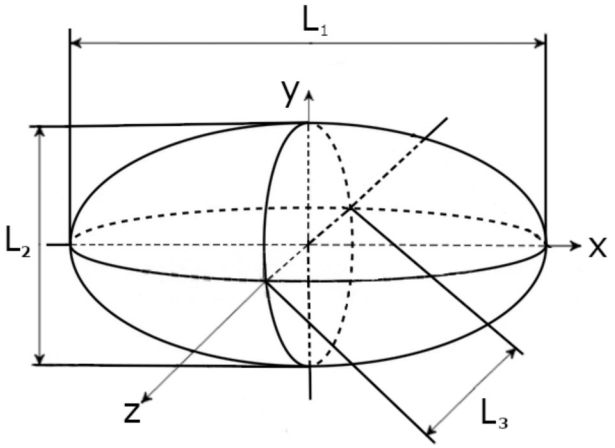

Fig. 1. Scheme of solid tumor with scalene ellipsoid geometry. L_1 (tumor major diameter), L_2 (tumor medium diameter) and L_3 (tumor minor diameter). The x, y and z axes are specified.

2. The parameter α^* changes in the time due to the necrosis and/or apoptosis induced into the solid tumor during and after EChT treatment [13,22,33,40,42,48,66,73,78].
3. The solid tumor is centered at the origin of the coordinate system and cancer cells flow from tumor center towards to its periphery [19].
4. Solid tumor is only formed by the cancer cells, whose total number is the sum of the numbers of viable tumor cells, dead cells and calcified cells, as assumed in [12].
5. The tumor is assumed spherical at $t = 0$ days, as we observe in preclinical studies [4,13,30,31,33]. In this case, all cancer cells concentrate in an initial cellular cluster without voids, as reported in [12].
6. The diffusion process is analyzed from the minimum experimentally measured tumor size. In preclinical studies, the initial tumor volume at $t = 0$ days may be any size higher and equal than the minimum measurable tumor volume [4,6,9,30,31,33].
7. A single DC stimulus during 30 min is applied when the solid tumor reaches its minimum measurable volume at $t = 0$ days. A single DC stimulus is often delivered to different histological varieties of tumors *in vitro* [37,39,46], preclinical [4,13,19,31,33,36,40,48,66,73,81] and clinical [42,78] studies.
8. The tumor irregular border, complex processes that occur in the boundary [19] and diffusion of cancer cells into the surrounding healthy tissue [31,33,81] are not considered in simulations. This may be argued from our experience in mice. We observe that Ehrlich, fibrosarcoma Sa-37 and F3II solid tumors (growing in BALB/c/Cenp and C57BL6/Cenp mice) exhibit regular borders for tumor volumes between 20 and 2000 mm^3. Therefore, L_1, L_2 and L_3 can be measured with vernier calipers. On the contrary, tumor irregular borders are observed for tumor volumes higher than 2000 mm^3 in these mice. Consequently, it is difficult to measure L_1, L_2 and L_3 [4,9,13,21,58].

Taking into account these assumptions, Eq. (1) can be extended to the case of an anisotropic tumors as

$$\frac{dv(\mathbf{x},t)}{dt} = \alpha^* v(\mathbf{x},t) - \beta v(\mathbf{x},t) ln \left| \frac{v(\mathbf{x},t)}{v_{ob}(\mathbf{x})} \right| + v(\mathbf{x},t) \frac{(\alpha^*)'}{\beta} \left(1 - e^{-\beta t}\right) + \nabla \left[\overline{D}(\mathbf{x}) \nabla v(\mathbf{x},t) \right], \tag{6}$$

where $\overline{D}(\mathbf{x})$ is the second order tensor of diffusion tumor, that we will assume symmetric and positive definite. The Eq. (6) allows us to know approximately how $v(\mathbf{x},t)$ maps change in terms of $t, \alpha, \beta, \nu, i/i_0$ ratio, and diffusion coefficients.

The $L^2 - norm$ of the density $v(\mathbf{x},t)$ given by

$$\|v(\mathbf{x},t)\|_{L^2(\Omega)} = \left[\int_\Omega |v(\mathbf{x},t)|^2 \, d\mathbf{x} \right]^{1/2}, \tag{7}$$

is sometimes called the total intensity of the function. It represents a mathematical measure of the "size" of the function and is related to the mass of the tumor. It will be useful for the study of the growth rate and boundedness of the tumor (see details in [5]).

2.3. Analysis of the model

In order to analyze the evolution of the solution, let us give first a Lemma.

Lemma 1. *If D is a symmetric and positive definite matrix, then*

$$-\mathbf{x}^T D\mathbf{x} \leq -v\|x\|_2^2 \tag{8}$$

where v, is the minimum eigenvalue of D.

Proof. See Appendix A.

Theorem 1. *Let $\Omega \in \mathbb{R}^3$ be an open set with smooth boundary. Let $v_0 \in W_o^{1,2}(\Omega)$. Let v be a solution to Eq. (6) which is assumed to be zero on the boundary Ω, that is, $v(\mathbf{x},t)|_{\partial\Omega=0}$. Then, the total intensity is bounded by*

$$\|v(\mathbf{x},t)\|_{L^2(\Omega)}^2 \leq e^{-bt}\|v(\mathbf{x},0)\|_{L^2(\Omega)}^2 + g(t)\|v_{ob}\|_{L^2(\Omega)}^2. \tag{9}$$

with

$$g(t) = e^{-bt}\int_0^t e^{bt}\beta e^{\frac{2c(t)}{\beta}}dt, \quad b = 2v\lambda_1^2 + \beta \quad \text{and} \quad c(t) = \alpha^* + \frac{(\alpha^*)'}{\beta}(1 - e^{-\beta t}). \tag{10}$$

Proof. See Appendix B.

Theorem 2. *When time tends to infinity we have*

$$\lim_{t\to\infty} g(t) = \lim_{t\to\infty} e^{-bt}\beta\int_0^t e^{bt}e^{\frac{2c(t)}{\beta}}dt \leq e^{\frac{2\alpha}{\beta}(a_1+a_2)} \tag{11}$$

Proof. See Appendix C.

Remark 1. From Theorem 1, it is clear that

$$\lim_{t\to\infty}\|v(\mathbf{x},t)\|_{L^2(\Omega)}^2 \leq \|v_{ob}(\mathbf{x},t)\|_{L^2(\Omega)}^2 \lim_{t\to\infty} g(t) \tag{12}$$

The function $g(t)$ does not tend to zero, and therefore we cannot ensure that the total intensity tends to zero. However, we can consider that the tumor remits if the limit of the total intensity is bounded by a small enough quantity. If we assume that we have full remission if the total intensity is smaller than a threshold ε, then this is guaranteed if

$$\lim_{t\to\infty} g(t)^{1/2} \leq e^{\frac{\alpha(a1+a2)}{\beta}} < \varepsilon\|v_{ob}\|_{L^2(\Omega)} \tag{13}$$

and this is obtained if

$$a_1 + a_2 < \frac{\beta}{\alpha}\ln\left(\varepsilon\|v_{ob}\|_{L^2(\Omega)}\right) \tag{14}$$

which gives us a sufficient condition on the ratio i/i_0 to get full remission of the tumor.

Two states for cancer cells are possible in vitro and in vivo studies: cancer cells exist or not. The existence of cancer cells is represented by $v(\mathbf{x},t)$ values different from zero. The non existence of cancer cells is represented by $v(\mathbf{x},t) = 0$, which makes the natural logarithm in Eq. (14) undefined. That is why, we chose 0.001 as the threshold value for $v(\mathbf{x},t)$ (see inequality Eq. (12)). In preclinical and clinical studies, this threshold value of $v(\mathbf{x},t)$ may represent the fibrous tissue that replaces that damaged (induction of necrosis and apoptosis) by DC cytotoxic

action [13,31,33,42]. Furthermore, very small value of this threshold for $v(\mathbf{x}, t)$ guarantees tumor destruction and avoids confusion with $v(\mathbf{x}, t)$ values in cancer.

The particular case where $\overline{D}(\mathbf{x})$ is proportional to the identity matrix represents the isotropic growth of a spherical solid tumor (observed at the first stages of TGK [9,30,31,33] and *in vitro* studies [79] and used in mathematical models [51,75] and its simulation is performed to confirm results documented in [5]). The tensor corresponding to this case is named $D_1(x)$. In preclinical studies, solid tumor adopt an ellipsoid geometry during their growth with three orthogonal diameters well defined L_1, L_2 and L_3 (see assumption 1 in Section 2.2).

Depending on the tumor histological variety and the host region where it grows, we observe two possibilities for the tumor growth: $L_1 > L_2 \gg L_3$ or $L_1 > L_2 > L_3$ [4,9,13,30,31,33,42], in accordance with other studies [36,40,48,51,66,71,73,78] and imaging techniques [56,65,66,69,72]. This indicates that diffusion along z axis for the case $L_1 > L_2 \gg L_3$ is slower than that for the case $L_1 > L_2 > L_3$. The tensor corresponding to the case $L_1 > L_2 \gg L_3$ is named $D_2(x)$ and the tensor corresponding to the case $L_1 > L_2 > L_3$ is named $D_3(x)$.

2.4. Numerical simulation

For simplicity we are going to consider that the tensor $\overline{D}(\mathbf{x})$ is diagonal. As the second-order tensor of diffusion is symmetrical and positive, there exists an orthonormal basis (which defines the principal axes of the medium) from which $\overline{D}(\mathbf{x})$ is represented by a diagonal matrix.

$$\overline{D}(\mathbf{x}) = \begin{bmatrix} D_{xx} & 0 & 0 \\ 0 & D_{yy} & 0 \\ 0 & 0 & D_{zz} \end{bmatrix}, \tag{15}$$

where D_{xx}, D_{yy} and D_{zz} are the main diagonal elements. The form of $\overline{D}(x)$ in Eq. (15) has been suggested in [21,70].

The Eq. (6) is numerically solved by the Method of Lines [57,64]. This method transforms the partial differential equation Eq. (6) into a system of ordinary differential equations. For the numerical calculation, the methodology reported in [5] is followed in this study. The simulations are made in a cube centered at the origin of the coordinate system, with sides equal to 8 mm. The domain considered is

$$\Omega = \left\{\mathbf{x} = (x, y, z) \in \mathbb{R}^3 : |x| \leq 4,\ \ |y| \leq 4, |z| \leq 4\right\}. \tag{16}$$

A uniform mesh in the spatial domain is made with a step $h = 0.08$ mm. A system of 10^6 ordinary differential equations is obtained. The explicit Runge–Kutta–Chebyshev method is proposed to solve this system [67]. It is a stabilized Runge–Kutta method for large nonlinear stiff systems of ordinary differential equations. In addition, the good stability of this method benefits from the stability function based on the first kind Chebyshev polynomials [67]. The integration domain has been taken large enough to guarantee that the density of the tumor is practically zero at the edges. That is why Dirichlet boundary conditions are established ($v(\mathbf{x}, t) = 0$ for $\mathbf{x} \in \partial\Omega$).

For the calculations the non existence of tumor volume at the point $\mathbf{x}$ is assumed when $v(\mathbf{x}, t) < 0.001$. Consequently, the tumor volume (in mm^3) in time t, named $V(t)$, and its mass (in g) in time t, named $M(t)$, are calculated from the following expressions

$$V(t) = \int_{\mathbf{x}\in\Omega, v(\mathbf{x},t)>0.001} 1 d\mathbf{x}, \qquad M(t) = \int_{\Omega} v(\mathbf{x}, t) d\mathbf{x}. \tag{17}$$

The initial conditions for $V(t)$ and $M(t)$ satisfy $V(t = 0) = V_o$ and $M(t = 0) = M_o$, respectively, where M_o is the initial tumor mass whereas V_o its initial volume. As the tumor volume is often used in the experiment, we establish the initial condition for this variable ($V_o = 20$ mm^3, whose initial radius (r_o) satisfies the initial condition $r_o = r(t = 0) = 1.6838$ mm). This tumor size is the minimum that we have measured in preclinical studies and observed at the TGK avascular phase. We observe that solid tumors keep spheroidal geometry for $20 \leq V_o \leq 50$ mm^3 [6,9,13,30,31,33]. As this tumor initial size is very small, we assume that $v(\mathbf{x}, t)$ reaches its maximum in the tumor center, named $max_x v(\mathbf{x}, t)$, and decays exponentially with the increase of sphere radius $r = (x^2 + y^2 + z^2)^{1/2}$, so that the condition $v(\mathbf{x}, t) < 0.001$ is satisfied outside the sphere. Taking into account these assumptions, the initial condition established for the numerical simulation is given by

$$v(\mathbf{x}, 0) = e^{-(x^2+y^2+z^2)/0{,}410478}. \tag{18}$$

Table 1
Values of model parameters for simulations.

Cases[a]	Values			
	γ(days^{-1})	D_{xx}	D_{yy}	D_{zz}
Case 1	0.02	0.08	0.08	0.0800
Case 2	0.02	0.80	0.13	0.0008
Case 3	0.02	0.80	0.13	0.0800
Case 4	1.00	0.08	0.08	0.0800
Case 5	1.00	0.80	0.13	0.0008
Case 6	1.00	0.80	0.13	0.0800

[a]For each Case, α(0.4 days^{-1}), β(0.2 days^{-1}) and i/i_0 ratio (0.0, 0.3, 1.5 and 2.25) are kept constants.

To simulate the tumor anisotropic growth we performed numerical simulations of the equations Eqs. (6) and (17). Each simulation case is identified with unique label in order to avoid repeating the list of parameter values. For this, six cases are proposed, named Case 1, Case 2, Case 3, Case 4, Case 5 and Case 6. For each of these cases, the values of γ, D_{xx}, D_{yy} and D_{zz} are shown in Table 1, keeping constant the values of α and β. In addition, four values of i/i_0 ratio (0.0, 0.3, 1.5 and 2.25) are used for simulations of Eq. (6). It should be noted that values of D_{xx}, D_{yy} and D_{zz} shown in Table 1 are not obtained from the experiment. These values were arbitrarily chosen to represent the anisotropy degree of the solid tumor, taking into account the different tumor geometries observed in the experiment: spheroid [58,79] (cases 1 and 4), scalene ellipsoid [13,40,50] (cases 3 and 6) and oblate ellipsoid [31,33] (cases 2 and 5). Taking into account theoretical and experimental results shown in [4–6,13,31,33], we simulate the untreated tumor growth for $i/i_0 = 0$ and three types of tumor responses after DC application: DP/SD (for $i/i_0 = 0.3$), PR (for $i/i_0 = 1.5$) and CR (for $i/i_0 = 2.25$). Furthermore, the time t is varied from 0 to 70 days in the graphs $V(t)$ versus t and $M(t)$ versus t because DC treated mice are cured from 50 days post-treatment, as reported experimentally in [6,13,31]. That is why, values of $v(\mathbf{x}, t)$ are not shown for $t \geq 50$ days. The spatial maps of $v(\mathbf{x}, t)$ are shown at $t = 0, 5, 10$ and 50 days.

A computer program was implemented in GNU fortran 95 to calculate the mass, volume and $v(\mathbf{x}, t)$ in the tumor. These quantities were obtained by approximating the integrals in (17) by sums by

$$V_h(t) \simeq \sum_{v_{ijk}>0.001} h^3, \quad M_h(t) \simeq \sum_{\Omega} v_{ijk}(t) h^3, \tag{19}$$

in a 4-core High-performance-computing (HPC) with 256 GB RAM of Instituto Universitario de Matemáticas y Aplicaciones (IUMA), Universidad de Zaragoza, Spain. All calculations took approximately 12 h.

3. Results

The graphs of $V(t)$ versus t (Fig. 2) and $M(t)$ versus t (Fig. 3) are obtained for Case 1 (Figs. 2, 3a), Case 2 (Figs. 2, 3b), Case 3 (Figs. 2, 3c), Case 4 (Figs. 2, 3d), Case 5 (Figs. 2, 3e) and Case 6 (Figs. 2, 3f). Figs. 2 and 3 reveal that time behaviors of $V(t)$ and $M(t)$ depend on γ value, i/i_0 ratio and anisotropy degree.

For $i/i_0 = 0.0$, $V(t)$ and $M(t)$ increase in the time up to an asymptotic value when the tumor grows isotropically (Figs. 2–3a,d). Nevertheless, these two physical quantities increase up to their respective maximum values and then decrease asymptotically when the tumor grows anisotropically (Figs. 2–3b,c,e,f), being marked for $D_{xx} = 0.8$, $D_{yy} = 0.13$ and $D_{zz} = 0.08$ (Figs. 2–3c,f). According Eq. (6), these time behaviors of $V(t)$ and $M(t)$ do not depend on γ parameter.

Depending on the values of γ, i/i_0 ratio, D_{xx}, D_{yy} and D_{zz}, we observe different time behaviors of $V(t)$ and $M(t)$ for $i/i_0 \neq 0.0$. As expected, volume and mass of the solid tumor follow similar trends in their temporal behaviors. For both time behaviors of $V(t)$ and $M(t)$, significant tumor growth delay, named TGD, is visualized when the γ value decreases, i/i_0 ratio increases and the tumor grows in its three directions, but not for $i/i_0 = 0.3$ (Figs. 2 and 3). Simulations reveal that TGD is observed for PR (for $i/i_0 = 1.5$) and CR (for $i/i_0 = 2.25$).

PR characterizes by an increase of tumor volume up to its maximum value and then it decreases in two different modes. First, tumor volume decreases until its minimum is reached and then it regrows (for $i/i_0 = 1.5$ in Figs. 2–3a,b,c). For this case, the tumor mass decreases until its minimum is reached and then it increases smoothly with

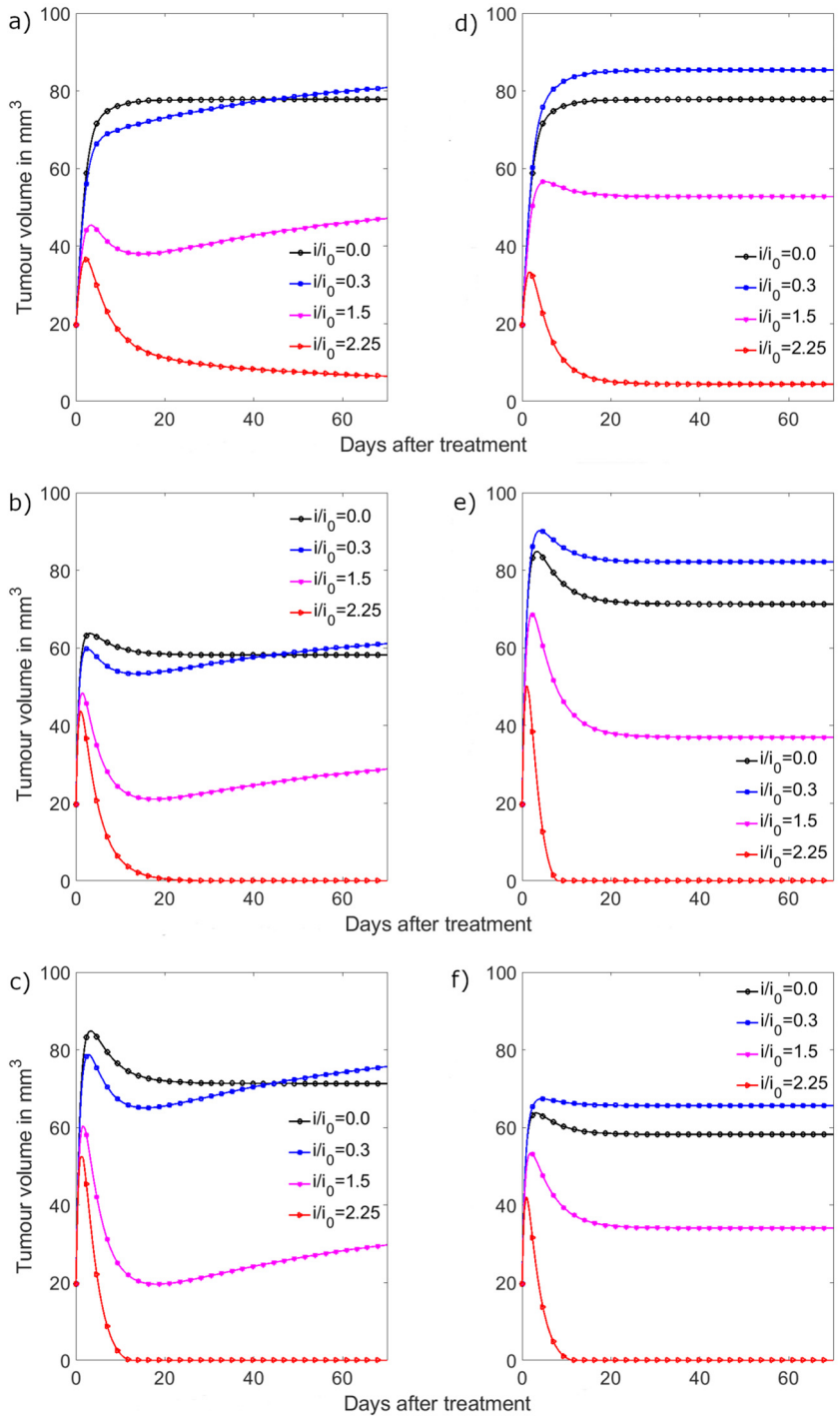

Fig. 2. Time behavior of tumor volume for (a) Case 1 ($\gamma = 0.02$ days^{-1} and $D_{xx} = D_{yy} = D_{zz} = 0.08$); (b) Case 2 ($\gamma = 0.02$ days^{-1}, $D_{xx} = 0.8$, $D_{yy} = 0.13$ and $D_{zz} = 0.0008$); (c) Case 3 ($\gamma = 0.02$ days^{-1}, $D_{xx} = 0.8$, $D_{yy} = 0.13$ and $D_{zz} = 0.08$); (d) Case 4 ($\gamma = 1$ days^{-1} and $D_{xx} = D_{yy} = D_{zz} = 0.08$); (e) Case 5 ($\gamma = 1$ days^{-1}, $D_{xx} = 0.8$, $D_{yy} = 0.13$ and $D_{zz} = 0.0008$) and (f) Case 6 ($\gamma = 1$ days^{-1}, $D_{xx} = 0.8$, $D_{yy} = 0.13$ and $D_{zz} = 0.08$). For each case, α(0.4 days^{-1}), β(0.2 days^{-1}) and i/i_0 ratio (0.0, 0.3, 1.5 and 2.25) are kept constants.

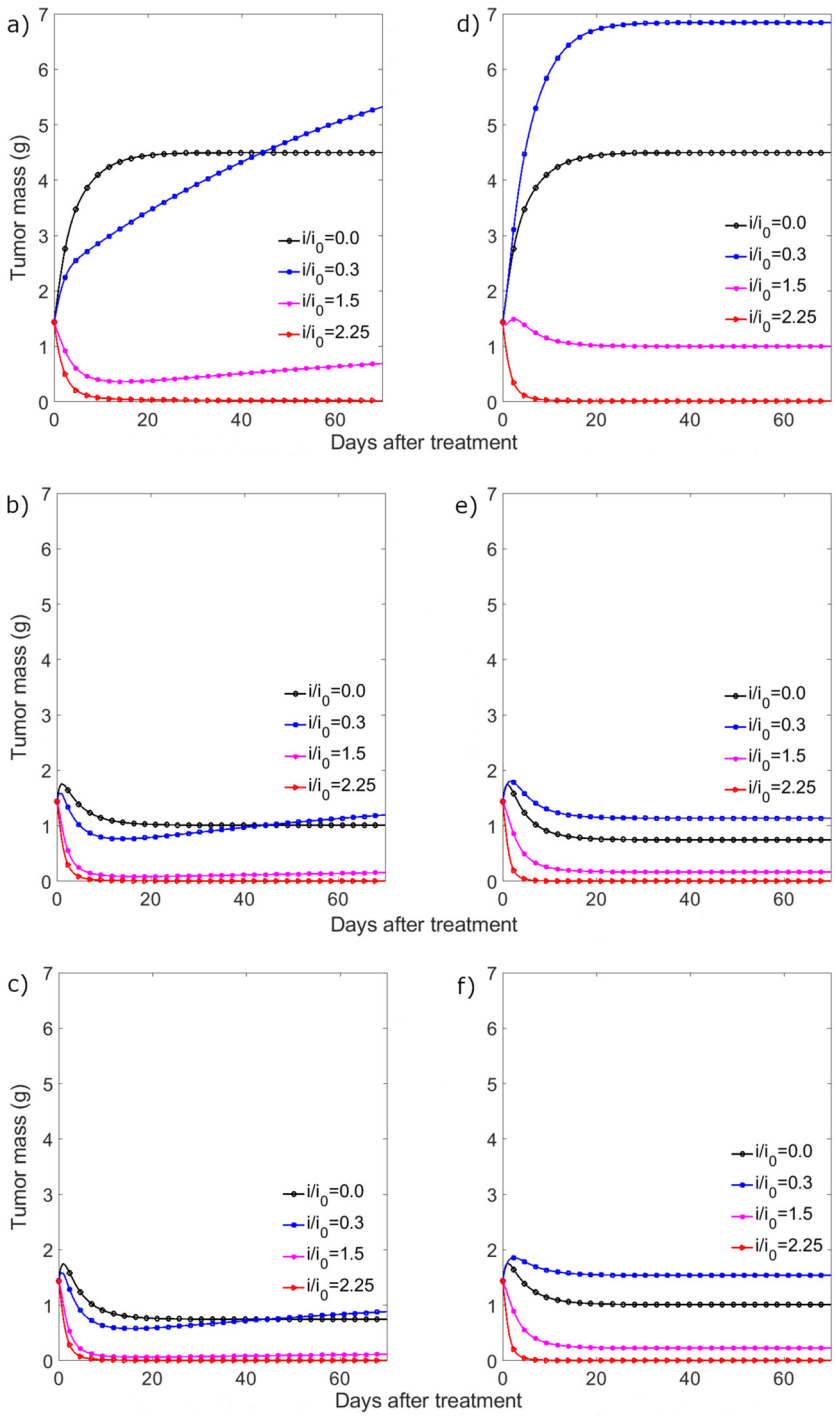

Fig. 3. Time behavior of tumor mass for (a) Case 1 ($\gamma = 0.02$ days^{-1} and $D_{xx} = D_{yy} = D_{zz} = 0.08$); (b) Case 2 ($\gamma = 0.02$ days^{-1}, $D_{xx} = 0.8$, $D_{yy} = 0.13$ and $D_{zz} = 0.0008$); (c) Case 3 ($\gamma = 0.02$ days^{-1}, $D_{xx} = 0.8$, $D_{yy} = 0.13$ and $D_{zz} = 0.08$); (d) Case 4 ($\gamma = 1$ days^{-1} and $D_{xx} = D_{yy} = D_{zz} = 0.08$); (e) Case 5 ($\gamma = 1$ days^{-1}, $D_{xx} = 0.8$, $D_{yy} = 0.13$ and $D_{zz} = 0.0008$) and (f) Case 6 ($\gamma = 1$ days^{-1}, $D_{xx} = 0.8$, $D_{yy} = 0.13$ and $D_{zz} = 0.08$). For each case, α(0.4 days^{-1}), β(0.2 days^{-1}) and i/i_0 ratio (0.0, 0.3, 1.5 and 2.25) are kept constants.

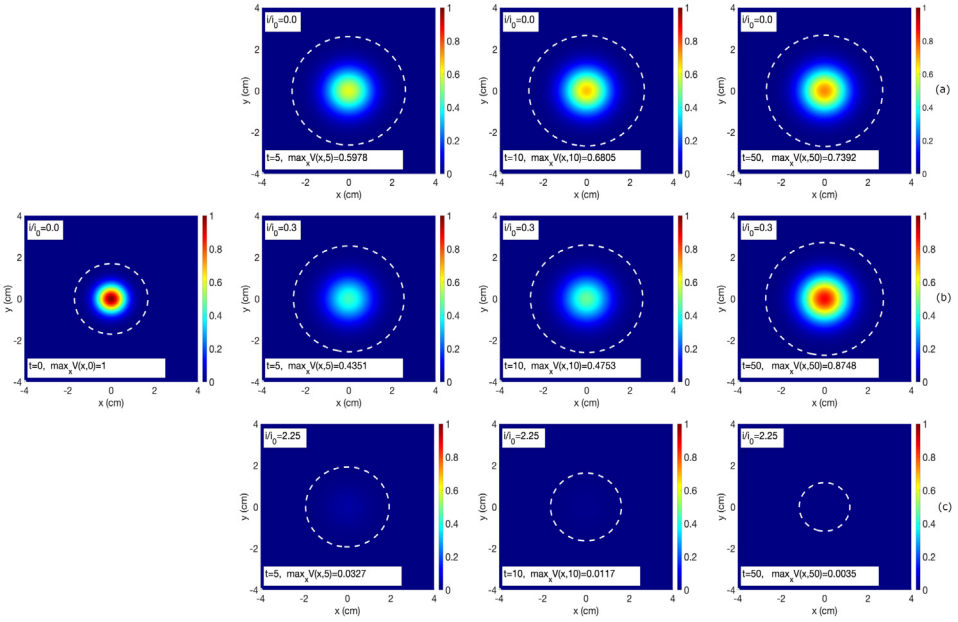

Fig. 4. Space–time map of tumor density for Case 1 ($\alpha = 0.4$ days^{-1}, $\beta = 0.2$ days^{-1}, $\gamma = 0.02$ days^{-1}, and $D_{xx} = D_{yy} = D_{zz} = 0.08$), four instants of time (0, 5, 10 and 50 days) and three values of i/i_0: (a) $i/i_0 = 0.0$. (b) $i/i_0 = 0.3$. (c) $i/i_0 = 2.25$. Dashed white line represents the tumor periphery.

time (Figs. 3a–c). Second, tumor volume decreases and then it tends asymptotically to a certain value (for $i/i_0 = 1.5$ in Figs. 2–3d,e,f). For this case, the tumor mass decreases asymptotically towards a certain value (Figs. 3d–f). CR characterizes by an initial increase of the tumor volume up to its maximum value and then it asymptotically decreases to zero, being noticeable for the tumor that grows in its three directions (Figs. 2a–f). Nevertheless, the tumor mass asymptotically decreases to zero (Figs. 3a–f).

Figs. 4–9 show the spatial maps of $v(\mathbf{x}, t)$ in (x, y, z) at $z = 0$ for Case 1 (Fig. 4), Case 2 (Fig. 5), Case 3 (Fig. 6), Case 4 (Fig. 7), Case 5 (Fig. 8) and Case 6 (Fig. 9) for four instants of time (0, 5, 10 and 50 days) and three values of i/i_0: $i/i_0 = 0.0$ (Figs. 4–9a), $i/i_0 = 0.3$ (Figs. 4–9b) and $i/i_0 = 2.25$ (Figs. 4–9c). In these figures, bright red, bright blue and white dashed line represent $max_x v(\mathbf{x}, t)$, the condition $v(\mathbf{x}, t) < 0.001$ and tumor periphery, respectively.

As expected for $i/i_0 = 0.0$ and $t = 0$, the maximum value of $v(\mathbf{x}, 0)$, named $max_x v(\mathbf{x}, 0)$, observes at the tumor center whereas values of $v(\mathbf{x}, 0) < 0.001$ are seen at the tumor periphery (Figs. 4–9), according to the initial condition assumed for $v(\mathbf{x}, 0)$ (Eq. (18)). For $i/i_0 = 0.0$ and $t > 0$, the $v(\mathbf{x}, t)$ values distribute in different isodense and concentric layers that adopt spherical or ellipsoidal geometry in the tumor that grows isotropically (Figs. 4, 5a) and anisotropically (Figs. 6–9a). As $v(\mathbf{x}, t)$ values do not depend on γ values for untreated tumors, the space–time maps of $v(\mathbf{x}, t)$ during the growth of these tumors are the same for Cases 1 and 4 (Figs. 4, 5a); Cases 2 and 5 (Figs. 6, 7a); and Cases 3 and 6 (Figs. 8, 9a). Geometries that adopt tumor diffusion depend on values of D_{xx}, D_{yy} and D_{zz}. We observe that $max_x v(\mathbf{x}, t)$ in the center and $v(\mathbf{x}, t)$ in each isodense-concentric spherical layer decrease in time when the untreated tumor grows anisotropically, being marked for the Case 3/Case 6. In contrast, $max_x v(\mathbf{x}, t)$ and $v(\mathbf{x}, t)$ values first decrease during isotropic growth of these untreated tumors (Figs. 4, 5a).

For $i/i_0 > 0.0$ and $t > 0$, the space–time maps and values of $v(\mathbf{x}, t)$ obtained for DC treated tumors differ from those for untreated tumors and depend on the values of i/i_0 ratio, γ, D_{xx}, D_{yy} and D_{zz} (Figs. 4–9b,c). For $i/i_0 = 0.3$ and keeping constant each value of D_{xx}, D_{yy} and D_{zz}, we see that space–time maps of $v(\mathbf{x}, t)$ adopt similar patterns to those for the untreated tumors (Figs. 4–9b). Higher $max_x v(\mathbf{x}, t)$ and $v(\mathbf{x}, t)$ values are observed for this i/i_0 ratio, being marked for the Case 4 (Fig. 5b). Furthermore, lower $max_x v(\mathbf{x}, t)$ and $v(\mathbf{x}, t)$ values are observed for the Case 3/Case 6 for this value of i/i_0 and maintaining constant the γ value, being slightly remarkable for $\gamma = 0.02$ days^{-1} during the first 10 days after DC application (Fig. 8 b). In contrast, $max_x v(\mathbf{x}, t)$ and $v(\mathbf{x}, t)$ values tend to zero in time for $i/i_0 = 2.25$ (Figs. 4–9c), being faster for the Cases 3 and 6 (Figs. 8, 9c).

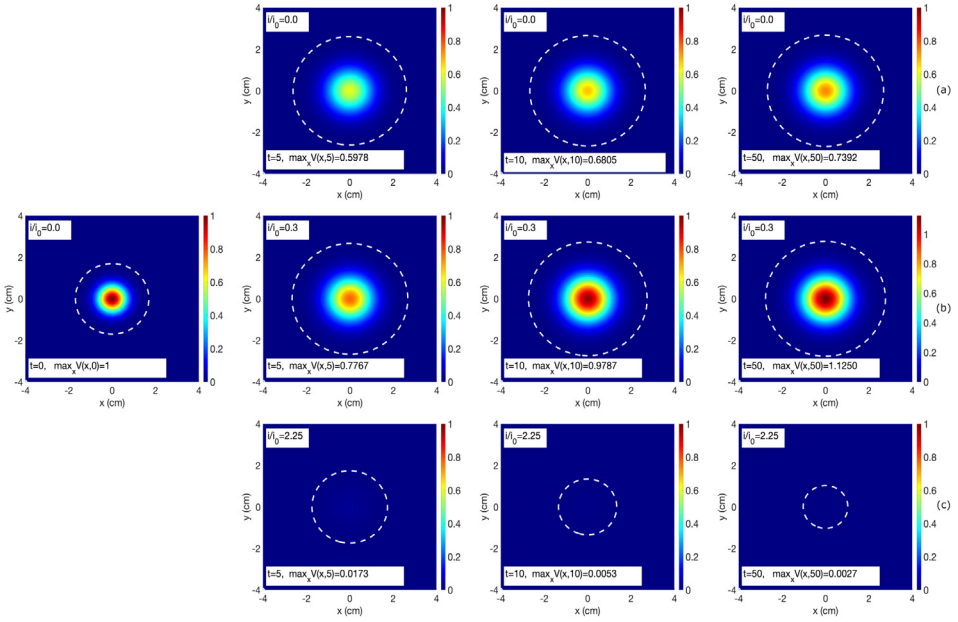

Fig. 5. Space–time map of tumor density for Case 4 ($\alpha = 0.4$ days^{-1}, $\beta = 0.2$ days^{-1}, $\gamma = 1$ days^{-1}, and $D_{xx} = D_{yy} = D_{zz} = 0.08$), four instants of time (0, 5, 10 and 50 days) and three values of i/i_0: (a) $i/i_0 = 0.0$. (b) $i/i_0 = 0.3$. (c) $i/i_0 = 2.25$. Dashed white line represents the tumor periphery.

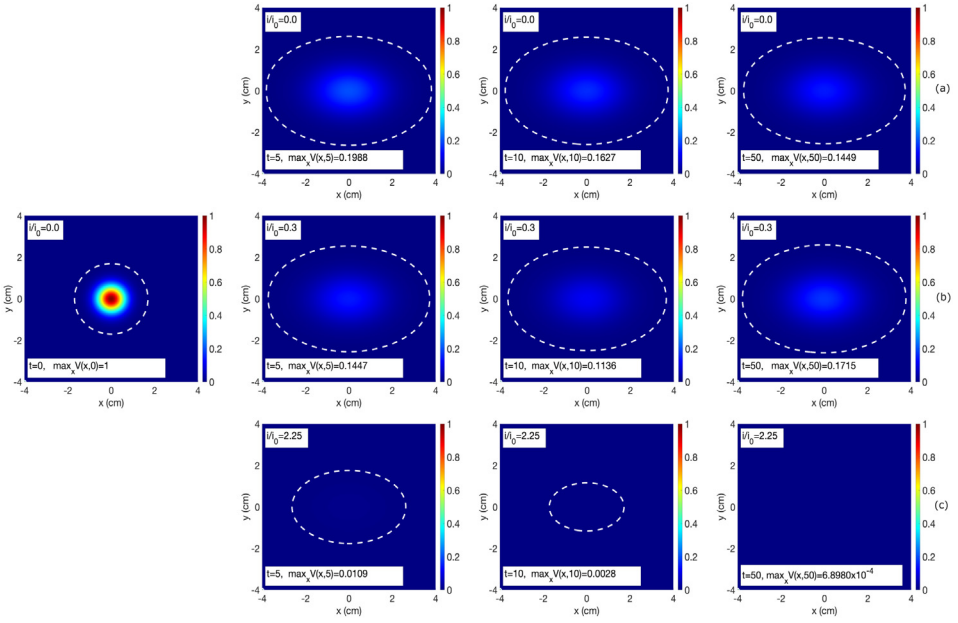

Fig. 6. Space–time map of tumor density for Case 2 ($\alpha = 0.4$ days^{-1}, $\beta = 0.2$ days^{-1}, $\gamma = 0.02$ days^{-1}, $D_{xx} = 0.8$, $D_{yy} = 0.13$ and $D_{zz} = 0.0008$), four instants of time (0, 5, 10 and 50 days) and three values of i/i_0: (a) $i/i_0 = 0.0$. (b) $i/i_0 = 0.3$. (c) $i/i_0 = 2.25$. Dashed white line represents the tumor periphery.

4. Discussion

Computed Axial Tomography (CT) allows differentiating hyperdense (white color), isodense (gray tones) and hypodense (black color) regions in cancer patients. CT protocols without contrast agents reveal that the necrosis,

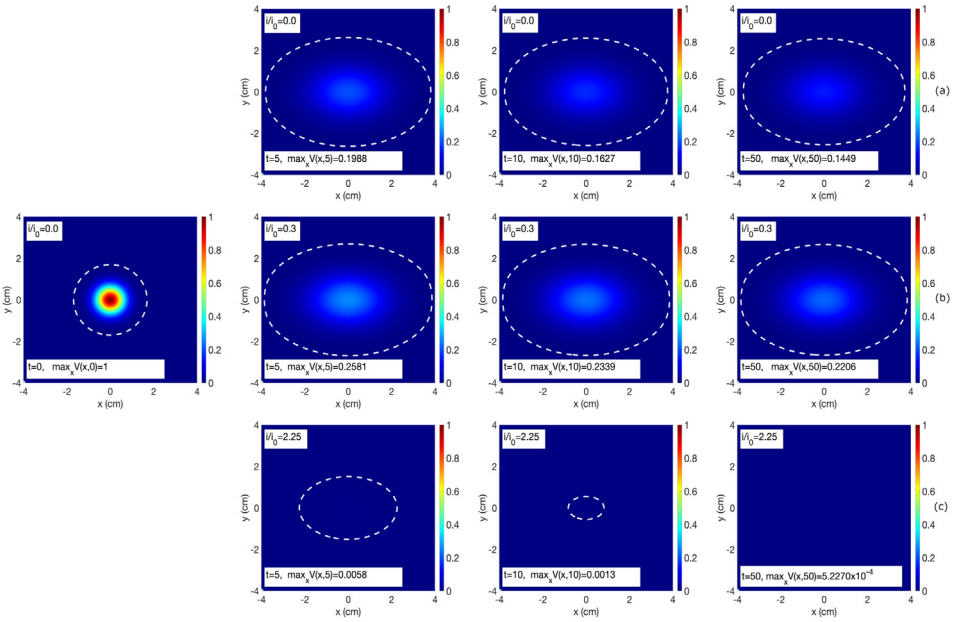

Fig. 7. Space–time map of tumor density for Case 5 ($\alpha = 0.4$ days^{-1}, $\beta = 0.2$ days^{-1}, $\gamma = 1$ days^{-1}, $D_{xx} = 0.8$, $D_{yy} = 0.13$ and $D_{zz} = 0.0008$), four instants of time (0, 5, 10 and 50 days) and three values of i/i_0: (a) $i/i_0 = 0.0$. (b) $i/i_0 = 0.3$. (c) $i/i_0 = 2.25$. Dashed white line represents the tumor periphery.

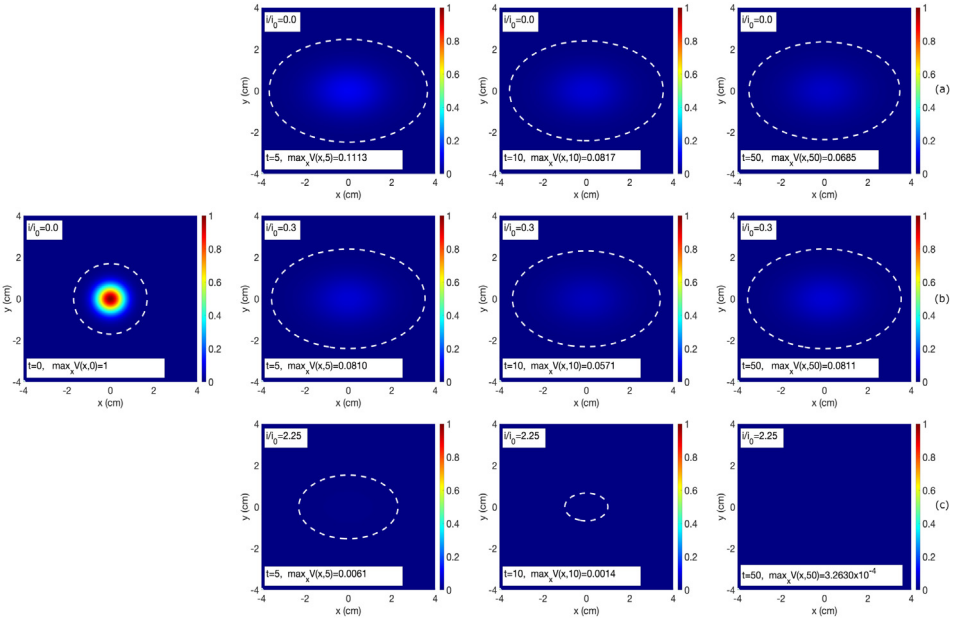

Fig. 8. Space–time map of tumor density for Case 3 ($\alpha = 0.4$ days^{-1}, $\beta = 0.2$ days^{-1}, $\gamma = 0.02$ days^{-1}, $D_{xx} = 0.8$, $D_{yy} = 0.13$ and $D_{zz} = 0.08$), four instants of time (0, 5, 10 and 50 days) and three values of i/i_0: (a) $i/i_0 = 0.0$. (b) $i/i_0 = 0.3$. (c) $i/i_0 = 2.25$. Dashed white line represents the tumor periphery.

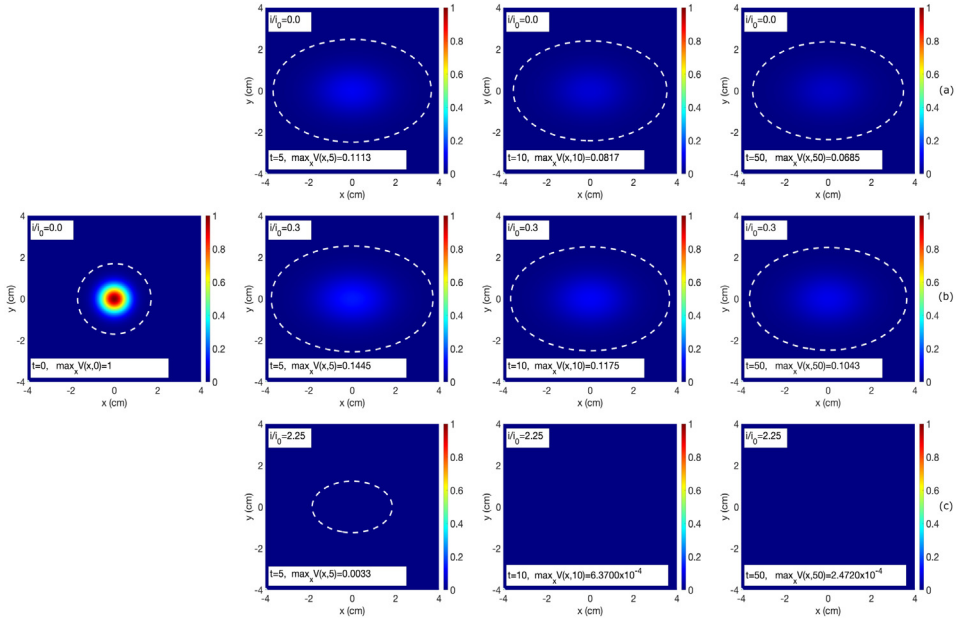

Fig. 9. Space–time map of tumor density for Case 6 ($\alpha = 0.4$ days^{-1}, $\beta = 0.2$ days^{-1}, $\gamma = 1$ days^{-1}, $D_{xx} = 0.8$, $D_{yy} = 0.13$ and $D_{zz} = 0.08$), four instants of time (0, 5, 10 and 50 days) and three values of i/i_0: (a) $i/i_0 = 0.0$. (b) $i/i_0 = 0.3$. (c) $i/i_0 = 2.25$. Dashed white line represents the tumor periphery.

water, fat, cancer parenchyma (made up of cancer cells that determine the tumor biologic behavior), blood vessels, edema and inflammation seem as hypodense zones whereas the bone, calcification, fibrosis and fresh blood appear as hyperdense regions. Nevertheless, blood vessels reveal themselves as hyperdense when contrast agents (i.e., iodine) are used in CT protocols [76,80]. In addition, in cancer patients we can observe that the solid tumor may be hyperdense or hypodense depending on the amount of blood. These imaging findings may be used to interpret the range of colors shown in the space–time maps of $v(\mathbf{x}, t)$ for untreated and DC treated solid tumors.

In analogy to CT imaging, we perform the bright red color ($v(\mathbf{x}, t) = 1$) as the most hyperdense regions of the tumor, corresponding in CT with the highest tissue density (e.g., the bone: $+2000\ UH$ and white color). The bright blue color ($v(\mathbf{x}, t) = 0$) depicts the tumor hypodense regions, equivalent in CT with lowest tissue density (e.g., the air: $-2000\ UH$ and dark color). The intermediate colors between red and blue show the tumorisodense regions, analogous in CT with the gray tones ($-2000\ UH < tissue\ density < +2000\ UH$). The value $v(\mathbf{x}, t) = 0.5$ (green color) may represent the value 0 (distilled water) notified in CT. Each isodense layer indicates tumor regions that contain cancer cells with their own phenotypic and genotypic characteristics.

4.1. Untreated tumor at $t = 0$

The main limitation of our model is that its results are not experimentally validated with imaging techniques (i.e., CT imaging or Imaging Nuclear Magnetic Resonance). Among other limitations may be mentioned, such as: (1) results shown in this study are valid if solid tumor is formed at a point in tissue/organ and then grows. (2) The model does not specify for which electrode array geometry the result is obtained. Despite these weaknesses, simulations of the tumor mass and volume behaviors mimic our previous experimental results [4,9,13,30,31,33] and give an approximated idea of cell diffusion and space–time distribution of density in cancer for different anisotropy degrees. Furthermore, our experience indicate that these behaviors are obtained for different DC intensities with various electrode array geometries. From these strengths of our model, we expose its main results for untreated and DC treated tumors.

At $t = 0$, the spatial map of $v(\mathbf{x}, 0)$ confirms the tumor spherical geometry, high intra-tumor heterogeneity and limited diffusion in space of the cancer cells at the avascular phase of TGK [15,51,74,75] and the first stages of

TGK [6,13,31,33]. High micro-heterogeneity and micro-anisotropy in tumors are suggested at very early stages of avascular phase of TGK [30]. At avascular phase of TGK, Cabrales et al. [6] suggest that central force fields are responsible of the spherical shape of the tumor. Nevertheless, Chen and Lowengrub [12] explain this spherical shape from the small duct radius and the static contact angle less than 90° between the cancer cell and basement membrane. This leads to the cell–cell adhesion (initial cellular packaging) because cancer cells prefer to adhere tightly to one another than to the basement membrane. Consequently, tumor layers spread faster. They explain tumor layers from small duct radius to guarantee the availability of nutrients and oxygen to the tumor cells.

The intra-tumor heterogeneity at avascular phase of TGK has been explained from the competence by nutrients, oxygen and space of cellular clusters formed by cancer cells with different phenotypic and genotypic characteristics [6,30]. From Eq. (18) and very small tumor size (20 mm^3), the intra-tumor heterogeneity shows the highest cell density in the tumor center, which is quantified by $max_x v(\mathbf{x}, t)$ and marked with bright red color. The highest cell density in the tumor center may be explained from hydroxyapatite microcalcification microstructures in the tumor [1,11,12,34,60] and the pre-existing vasculature in the stroma [12].

Although mechanisms for which the microcalcifications form are unknown [60], it has been suggested that they generate when calcium leaves in the cancer cells (calcified cells), via apoptosis and/or necrosis, because of lack of nutrients and oxygen [12,13,30]. Consequently, they calcify due to fluid volume loss [12]. Bright red color (tumor cell) in the map of $v(\mathbf{x}, 0)$ may corroborate results of Chen and Lowengrub [12], who document that calcified cells tend to form a solid-like mass within the tumor and they diffuse more slowly than other cell types. This may explain why calcified cells concentrate in the tumor center and cells that are actively proliferating migrate towards the tumor periphery. In simulations, these proliferating cells are marked with the dark blue color, whose $v(\mathbf{x}, 0)$ values correspond to the interval $0.01 < v(\mathbf{x}, 0) < 0.3$.

4.2. Untreated tumor growth kinetics

Chen and Lowengrub [12] report that larger adhesion between tumor cells and the basement membrane occurs for large contact angles, which are related to more concave shape, faster growth and greater elongation of the untreated solid tumor in time. This facilitates that more tumor cells access to nutrients and oxygen, and the tumor contour spreads much faster. Elongated untreated tumors are often observed in preclinical [4,6,9,13,30,31,33] and clinical [18,42,78] studies, and corroborated in simulations of $V(t)$, $M(t)$ and $v(\mathbf{x}, 0)$ for $t > 0$, $i/i_0\ ratio = 0.0$, $D_{xx} = 0.8$, $D_{yy} = 0.13$ and $D_{zz} = 0.08$. These aspects may explain why the cancer cells distribute in several concentric, very poor differentiated and flattened ellipsoid-shaped layers with lowest $max_x v(\mathbf{x}, t)$, and $v(\mathbf{x}, t)$ values (lower density) during its growth. We hypothesize that $v(\mathbf{x}, t)$ values of multiple layers may be related to the untreated cancer differentiation grade. Very similar values of $v(\mathbf{x}, t)$ among layers may simulate undifferentiated (Grade 4) or badly differentiated (Grade 3) tumors, which are very aggressive and metastatic. In addition, layers with different $v(\mathbf{x}, t)$ values may represent poorly differentiated cancer, in agreement with Bertoni et al. [2].

Heterogeneous multiple ellipsoidal layers in space–time maps of $v(\mathbf{x}, t)$ confirm that the most heterogeneous and anisotropic untreated solid malignant tumors grow faster, as confirmed experimentally in aggressive malignant tumors (for example, sarcoma, fibrosarcoma, glioma and glioblastoma multiforme) [14,18,21,31,33,56]. Furthermore, the heterogeneity and anisotropy of solid tumors have been related to their resistance to anticancer therapies [10,16,37,56,76].

A decrease in intra-tumor density means that the tumor is softer, which leads to macroscopic deformations [11]; instabilities, intrinsic dynamic structural transformations, fractality and geometry changes [9,30,32]; the stochastic nature [25]; among others [30,31,50] involved in untreated solid tumor during its growth. Additionally, Fenner et al. [24] report a strong correlation between the macroscopic deformation of the tumor, the deformation of its cells at the microscopic level and the spread of metastasis, suggesting that the overall hardness of a tumor does not necessarily correlate with its aggressiveness, invasion and metastasis, in accordance with the simulations shown in this study for the greater degree of tumor anisotropy. The change of the spheroid to ellipsoidal geometry of the untreated tumor is observed in preclinical studies [4,6,13,30,31,33] and related to the jump from the avascular phase to the vascular phase of the TGK [6,30]. This jump may correspond to the maximum values of volume and mass of the untreated tumor, being marked for the solid tumor that grows with unequal diameters (three diameters well defined), in agreement with [30].

Unlike tumor that grows anisotropically, well-defined multilayers are observed in the spherical tumor, in which $max_x v(\mathbf{x}, t)$ in the tumor center increases during its growth (represented with the faint red color). This red color may

be explained from the formation of calcified cells due to the central necrosis resulting from a lack of nutrients and oxygen in the central region of the untreated tumor during its growth, in agreement with [13]. This is marked for the tumor that grows spherically because its well-defined layers offer more resistance to the passage of nutrients and oxygen towards the tumor center, a manner that agree with results of Chen and Lowengrub [12]. We do not rule out that the red color associated to the $max_x v(\mathbf{x}, 50)$ may be influenced by the tumor fibrosis due to reparative or reactive process associated with physiological central necrosis. The fibrosis causes an increase in collagen production, which explains the hyperdensity of fibrous tissue [12].

In contrast, the blue color observed in space–time maps of $v(\mathbf{x}, t)$ may be explained by the migration of cancer cells from tumor center to its periphery and new blood vessels (process known as endogenous angiogenesis) arranged at the tumor surface during its growth, being marked for untreated tumor growths with $D_{xx} = 0.8$, $D_{yy} = 0.13$ and $D_{zz} = 0.08$, as reported in [12,51]. This may explain the untreated solid tumor radial growth and why its greater electro-physiological activity is concentrated in regions near its periphery, in accordance with [37,73]. As a result, a question can be asked: Is intra-tumor central necrosis derived from radial diffusion of cancer cells or lack of oxygen and nutrients, or both?

The range of colors from red to blue in space–time maps of $v(\mathbf{x}, t)$ may correspond with the space-dependent blood perfusion reported by Lodi et al. [49]. These authors suggest that the tumor vascular architecture results in a blood perfusion that decreases suddenly from the tumor periphery to its center. We assume that tumor zones with higher blood perfusion may correspond to blue color in space–time maps of $v(\mathbf{x}, t)$, whereas tumor zones with low blood perfusion with the red color, as its center. Blood vessels are seen as hypodense zones in CT [76,80]. This confirms the large inhomogeneous vascularization in solid tumors in agreement with Lodi et al. [49].

Although simulations are not shown, the findings reported in this study for untreated tumors become even more noticeable when α increases with respect to β, which confirms that the tumor histological variety also has a fundamental role in its growth, as documented in [6,13,30,31,33]. A close relationship of α and β with the fractal dimensions of the mass and contour of a solid tumor is reported in [9]. In addition, these parameters are linked to the coefficients of Avrami formulations [5].

4.3. Direct current treated tumor growth kinetics

Previous studies suggest that the tumor response type after DC application depends on the i/i_0 ratio, the histological variety of the tumor (α and β values) and the duration of the DC-induced antitumor effect (inverse of γ) [5,6,13,31,33,39]. González et al. [31] report experimentally that each DC treated tumor response type depends also on the exposure time of the DC. Nevertheless, the simulations of this study demonstrate that it depends not only on these parameters, but also on intra-tumor heterogeneity (space–time map of $v(\mathbf{x}, t)$) and the degree of intra-tumor anisotropy (values of D_{xx}, D_{yy} and D_{zz}). The fastest decrease of $M(t)$, $V(t)$, $max_x v(\mathbf{x}, t)$ and $v(\mathbf{x}, 50)$ in time corresponding to the greater value of i/i_0, lower value of γ and the greater degree of anisotropy of the tumor confirm that most heterogeneous, anisotropic and aggressive tumors are the most sensitive to DC action, in accordance with previous studies [4,31,33].

The space–time extension of decrease of $v(\mathbf{x}, t)$ in the tumor (hypodense region identified in blue color) and time decreases of $M(t)$, $V(t)$, $max_x v(\mathbf{x}, t)$ and $v(\mathbf{x}, t)$ values confirm the increase in space–time of the DC treated tumor destruction observed in simulations [7,8,66], potato pieces [8,29], *in vitro* [39], preclinical [13,22,48,66] and clinical [42,78] studies. This aspect is confirmed by fluorescence imaging [62] and pathological anatomy [13,22]. In addition, this decrease in the time of $max_x v(\mathbf{x}, t)$ and $v(\mathbf{x}, t)$ values in ellipsoidal tumors may be due to the coagulative necrosis around the anode (necrosis caused by ischemia and causing the appearance of fibrous tissue) and liquefactive necrosis around the cathode (type of necrosis that results in a transformation of the tumor into a liquid viscous mass) induced by DC action [13,42]. A criterion to stop the DC application is when the tumor texture changes from hard to soft or from soft to softer, depending on the tumor histological variety [42,78].

The tendency to zero of $M(t)$, $V(t)$, $max_x v(\mathbf{x}, t)$ and $v(\mathbf{x}, t)$ values for $i/i_0 \geq 2.25$ confirms theoretically the existence of $(i/i_0)_{th}$, from which the CR of the tumor can be achieved (most dark blue) for any value of γ, degree of tumor anisotropy and diffusion geometry (spherical or ellipsoidal), as reported theoretically [4,6] and experimentally in preclinical studies (mice bearing Ehrlich tumor, fibrosarcoma Sa-37 [4,13], and breast carcinoma F3II [31,33] other tumor histological varieties [22,36,39,40,48,66]; and in clinical studies [36,42,78]).

In contrast, quick growths of $M(t)$, $V(t)$, $max_x v(\mathbf{x}, t)$ and $v(\mathbf{x}, t)$ values are observed for $i/i_0 < (i/i_0)_{th}$, the highest value of γ and the lower degree of tumor anisotropy. This aspect is notable for the lower value of i/i_0 and corroborates that very small DC intensities may stimulate the tumor growth compared to that of the untreated tumor, a matter that agrees with [4]. In this case, the increases of $max_x v(\mathbf{x}, t)$ and $v(\mathbf{x}, t)$ values during and after DC treatment (red color) explain the increase of the tumor density (hyperdense regions) by ischemia–reperfusion, necrosis and apoptosis induced by this physical therapy. This tissue damage leads to the fibrous tissue observed days after DC treatment [6,13,31,33,42] and the formation of calcified cells [1,11,12,34,60].

It can be verified that other values of γ, D_{xx}, D_{yy} and D_{zz} to those shown in Table 1 do not change the simulation results for volume, mass and density of the solid tumor when $i/i_0 \geq 2.25$. This does not happen for $0 < i/i_0 < 2.25$. For this case, higher growth delays of three physical magnitudes are observed for the lower values of γ (< 0.02 days^{-1}) and greater values of i/i_0, being marked when D_{xx} increases respect to D_{yy}, and at the same time D_{yy} increases regards to D_{zz}. These results confirm the existence of an i/i_0 threshold value, as suggested in previous studies from theoretically [4] and experimentally [13,31,33] points of view.

The results of this study and those reported in [4–6,13,30,31,33] suggest the need to know in depth the ratio i/i_0, in terms of the therapy parameters (i, exposure time, number of application and geometry of the array of electrodes), the variable γ, the ratio α/β, the degree of anisotropy of the tumor, tumor fractal dimensions (tumor mass and its contour), biological and electrical microenvironment, and the variable that describes cellular loss mechanisms. For this, results reported in [9,19,27,30,32,55] should be considered. This will permit to establish and customize the value of (i/i_0) so that the EChT makes the cancer reach always its SPR or CR in an organism, as proposed in [4,6].

4.4. Future works and research directions

One limitation of the present study is that the model has not been tested with data of real tumors. With the presented simulations we can deduce that the model provides correct information about the time evolution of the tumor. Obtaining data of the evolution of the density of tumors and fitting the parameters of the model to this data will give valuable information.

Despite its limitations, this study focused on knowing how at first approximation the anisotropy degree influence in volume, mass and density in both unperturbed and DC perturbed tumors during their growths. The mathematical formalism shown here generalize that reported by Cabrales et al. [5]. These simulations in both studies are valid if the solid tumor originates from a unique cellular clone and grows monofocally in a single organ (i.e., cancers of breast and liver). Nevertheless, multifocal and multicentric breast cancer are observed in clinics. Multifocal breast cancer is defined when there is more than one distinct tumor within the same quadrant of this tissue. Multicentric breast cancer is defined when cancers develop in different quadrants of this tissue [54]. At present, the same ideas of this study are being implemented to multifocal and multicentric solid tumors to know approximately how the anisotropy degree influence in volume, mass and density of both unperturbed and DC perturbed tumors during their growths.

The simulations of this study and those reported in [5] do not explicitly take into account the information of different geometries of electrode arrays for the treatment of solid tumors when DC is applied [31,33,36,59]. We are developing a further study to include these electrode array geometries in the formalism shown here. Other ideas for the validation of $v(\mathbf{x}, t)$ maps are being developed taking into account real data of densities (measured in images obtained with TAC) or intensities (measured in images obtained with imaging nuclear magnetic resonance) from different parts in a solid tumor. This will solve one of the limitations of this study: $v(\mathbf{x}, t)$ maps are not experimentally verified.

The ideas of this study will be extended to other equations used to describe TGK [9,30,32]. For this, DC parameters and diffusion term will be introduced in these equations, which reveal several findings that differ from those reported with MGE and MGE-d.

5. Conclusions

We have proposed a model for anisotropic tumor growth. This has been theoretically analyzed obtaining conditions on the parameters, that guarantee the limits of the solutions and allow to deduce conditions in which the tumor remits under the effect of EChT. The simulations of this model allowed obtaining spatio-temporal maps of

the distribution of mass, volume and density for each type of response after applying DC. These results show that the greatest DC antitumor effectiveness occurs for the greatest ratio i/i_0 and the highly heterogeneous, anisotropic, aggressive and hypodense malignant solid tumors.

Acknowledgments

Authors gratefully acknowledge useful comments and invaluable feedback provided by Editor in Chief and two unknown reviewers. Consequently, this manuscript is significantly improved. Furthermore, we thank to Yenia Infantes Frómetas for her valuable assistance in correction to the English manuscript. This research is supported by the doctoral scholarship from the Universidad de Zaragoza-Santander Universidades program, Spain and the projects PID2019-109045GB-C31 of Ministery of Science and Innovation of Spain. Furthermore, this research is partially supported by the CITMA de Santiago de Cuba, Cuba (Project PT241SC003-002).

Appendix A. Proof of Lemma 1

Proof. Since D is symmetric and positive definite matrix, there exist an orthogonal matrix Q that leads D to diagonal form. Moreover, the eigenvalues of D are real and positive

$$D = Q^T C Q \quad with \quad C = \begin{bmatrix} \lambda_1 & 0 & 0 \\ 0 & \lambda_2 & 0 \\ 0 & 0 & \lambda_3 \end{bmatrix}.$$

Then,

$$\frac{\mathbf{x}^T D\mathbf{x}}{\mathbf{x}^T\mathbf{x}} = \frac{\mathbf{x}^T Q^T C Q\mathbf{x}}{\mathbf{x}^T Q^T Q\mathbf{x}} = \frac{Y^T C Y}{Y^T Y},$$

Consequently,

$$inf_{\mathbf{x}\neq 0}\ \frac{\mathbf{x}^T D\mathbf{x}}{\mathbf{x}^T\mathbf{x}} = inf\frac{Y^T C Y}{Y^T Y} = inf\frac{\lambda_1 y_1^2 + \lambda_2 y_2^2 + \lambda_3 y_3^2}{y_1^2 + y_2^2 + y_3^2} \geq min\{\lambda_1, \lambda_2, \lambda_3\} = \nu,$$

and it is obtained

$$\mathbf{x}^T D\mathbf{x} \geq \nu \mathbf{x}^T\mathbf{x}. \tag{A.1}$$

Appendix B. Proof of Theorem 1

Proof. If both sides of Eq. (6) are multiplied by $v(\mathbf{x}, t)$, the following equation results

$$\begin{aligned} v(\mathbf{x},t)\frac{dv(\mathbf{x},t)}{dt} &= \alpha^* v^2(\mathbf{x},t) - \beta v^2(\mathbf{x},t) ln\left|\frac{v(\mathbf{x},t)}{v_{ob}(\mathbf{x})}\right| + v^2(\mathbf{x},t)\frac{(\alpha^*)'}{\beta}\left(1 - e^{-\beta t}\right) \\ &\quad + v(\mathbf{x},t)\nabla\left[\overline{D}(\mathbf{x})\nabla v(\mathbf{x},t)\right] \end{aligned} \tag{B.1}$$

Integrating on both sides,

$$\begin{aligned} \frac{1}{2}\frac{d}{dt}\int_\Omega |v(\mathbf{x},t)|^2 dx &= \alpha^* \int_\Omega |v(\mathbf{x},t)|^2 dx - \beta \int_\Omega |v|^2 ln\left|\frac{v(\mathbf{x},t)}{v_{ob}(\mathbf{x})}\right| dx \\ &\quad + \frac{(\alpha^*)'}{\beta}\left(1 - e^{-\beta t}\right)\int_\Omega v^2(\mathbf{x},t) dx \\ &\quad + \int_\Omega v(\mathbf{x},t)\nabla\left[\overline{D}(\mathbf{x})\nabla v(\mathbf{x},t)\right]. \end{aligned} \tag{B.2}$$

Applying the following vector identity

$$\nabla\cdot\left[v(\mathbf{x},t)\cdot\overline{D}(\mathbf{x})\nabla v(\mathbf{x},t)\right] = \nabla v(\mathbf{x},t)\cdot\left(\overline{D}(\mathbf{x})\nabla v(\mathbf{x},t)\right) + v(\mathbf{x},t)\nabla\cdot\left(\overline{D}(\mathbf{x})\nabla v(\mathbf{x},t)\right), \tag{B.3}$$

it is obtained

$$\begin{aligned}\frac{1}{2}\frac{d}{dt}\int_{\Omega}|v(\mathbf{x},t)|^2dx = &\left[\alpha^* + \frac{(\alpha^*)'}{\beta}\left(1-e^{-\beta t}\right)\right]\int_{\Omega}|v(\mathbf{x},t)|^2dx\\ &-\beta\int_{\Omega}|v(\mathbf{x},t)|^2 ln\left|\frac{v(\mathbf{x},t)}{v_{ob}(\mathbf{x})}\right|dx\\ &+\int_{\Omega}\nabla\cdot\left[v(\mathbf{x},t)\cdot\overline{D}(\mathbf{x})\nabla v(\mathbf{x},t)\right]dx\\ &-\int_{\Omega}\nabla v(\mathbf{x},t)\cdot\left(\overline{D}(\mathbf{x})\nabla v(\mathbf{x},t)\right)dx.\end{aligned} \tag{B.4}$$

Denoting by ν the minimum eigenvalue of the matrix $\overline{D}(\mathbf{x})$ (recall that it is positive definite and therefore their eigenvalues are all positive), and using Lemma 1, we have

$$-\nabla v(\mathbf{x},t)\cdot\left(\overline{D}(\mathbf{x})\nabla v(\mathbf{x},t)\right) \leq -\nu|\nabla v(\mathbf{x},t)|^2. \tag{B.5}$$

In this way, it is obtained that

$$-\int_{\Omega}\nabla v(\mathbf{x},t)\cdot\left(\overline{D}(\mathbf{x})\nabla v(\mathbf{x},t)\right)dx \leq -\nu\int_{\Omega}|\nabla v(\mathbf{x},t)|^2dx. \tag{B.6}$$

Furthermore, as $v(\mathbf{x},t)=0$ at the boundary, it results

$$\begin{aligned}\frac{1}{2}\frac{d}{dt}\int_{\Omega}|v(\mathbf{x},t)|^2dx \leq &\left[\alpha^* + \frac{(\alpha^*)'}{\beta}\left(1-e^{-\beta t}\right)\right]\int_{\Omega}|v(\mathbf{x},t)|^2dx\\ &-\beta\int_{\Omega}|v(\mathbf{x},t)|^2 ln\left|\frac{v(\mathbf{x},t)}{v_{ob}(\mathbf{x})}\right|dx - \nu\int_{\Omega}|\nabla v(\mathbf{x},t)|^2dx.\end{aligned} \tag{B.7}$$

Inequality of Poincaré [23] states that

$$|v|_{L^2(\Omega)} \leq C_p|\nabla v|_{L^2(\Omega)}. \tag{B.8}$$

From the theorem of Rayleigh quotient [68], the best constant in this inequality is the lower eigenvalue of the Laplacian operator $C_p = \lambda_1^{-1}$,resulting

$$\int|v|^2dx \leq \lambda_1^{-2}\int|\nabla v|^2dx \tag{B.9}$$

Consequently,

$$\begin{aligned}\frac{1}{2}\frac{d}{dt}\int_{\Omega}|v(\mathbf{x},t)|^2dx \leq &\left[\alpha^* + \frac{(\alpha^*)'}{\beta}\left(1-e^{-\beta t}\right)\right]\int_{\Omega}|v(\mathbf{x},t)|^2dx\\ &-\beta\int_{\Omega}|v(\mathbf{x},t)|^2 ln\left|\frac{v(\mathbf{x},t)}{v_{ob}(\mathbf{x})}\right|dx - \nu\lambda_1^2\int_{\Omega}|v(\mathbf{x},t)|^2dx.\end{aligned} \tag{B.10}$$

This equation can be rewritten as

$$\begin{aligned}\frac{1}{2}\frac{d}{dt}\int_{\Omega}|v(\mathbf{x},t)|^2dx \leq &\int_{\Omega}|v(\mathbf{x},t)|^2\left[c(t)+\frac{\beta}{2}-\beta ln\left|\frac{v(\mathbf{x},t)}{v_{ob}(\mathbf{x})}\right|\right]dx\\ &-\left(\nu\lambda_1^2+\frac{\beta}{2}\right)\int_{\Omega}|v(\mathbf{x},t)|^2dx,\end{aligned} \tag{B.11}$$

if $s = v(\mathbf{x},t)$, $u = c(t)+\frac{\beta}{2}$ and $s_0 = v(\mathbf{x},0)$ is obtained the following function

$$f(s) = s^2\left(u-\beta ln\frac{s}{s_0}\right). \tag{B.12}$$

The maximum of $f(s)$ is obtained by means of the computation of the first derivate $f'(s)$, given by

$$f'(s) = -s\left(2\beta ln\frac{s}{s_0} - 2u + \beta\right) = 0, \tag{B.13}$$

being the maximum

$$s_1 = s_0 e^{\frac{u}{\beta}-\frac{1}{2}}. \tag{B.14}$$

Substituting this maximum in the original expression for $f(s)$, gives

$$f(s_1) = s_0^2\frac{\beta}{2}e^{\frac{2u}{\beta}-1}. \tag{B.15}$$

In this way, the following condition can be established

$$s^2\left(u - \beta ln\frac{s}{s_0}\right) \leq s_0^2\frac{\beta}{2}e^{\frac{2u}{\beta}-1}. \tag{B.16}$$

Consequently,

$$|v(\mathbf{x},t)|^2\left[c(t) + \frac{\beta}{2} - \beta ln\left|\frac{v(\mathbf{x},t)}{v_{ob}(\mathbf{x})}\right|\right] \leq |v_{ob}(\mathbf{x})|^2\frac{\beta}{2}e^{\frac{2c(t)}{\beta}}. \tag{B.17}$$

Therefore, it can be written that

$$\begin{aligned}\frac{d}{dt}\int_\Omega |v(\mathbf{x},t)|^2dx &\leq \beta e^{\frac{2c}{\beta}}\int |v_{ob}(\mathbf{x})|^2dx - 2\left(\nu\lambda_1^2 + \frac{\beta}{2}\right)\int_\Omega |v(\mathbf{x},t)|^2dx \\ &= a(t)\int |v_{ob}(\mathbf{x})|^2dx - b\int_\Omega v(\mathbf{x},t)|^2dx,\end{aligned} \tag{B.18}$$

where

$$a(t) = \beta e^{\frac{2c(t)}{\beta}}, \quad b = 2\nu\lambda_1^2 + \beta.$$

It may be argued that the square of the total intensity is bounded by the solution of the following non-homogeneous differential equation of constant coefficients

$$y' = a(t)y_{ob} - by. \tag{B.19}$$

Then, the following boundedness is satisfied

$$\int |v(\mathbf{x},t)|^2dx \leq e^{-bt}\int |v_0(\mathbf{x},t)|^2dx + g(t)\int |v_{ob}(\mathbf{x},t)|^2dx \qquad .\forall t \tag{B.20}$$

with

$$a(t) = \beta e^{\frac{2c(t)}{\beta}}, \qquad b = 2\nu\lambda_1^2 + \beta, \qquad g(t) = e^{-bt}\int_0^t a(t)e^{bt}dt. \tag{B.21}$$

Recall that

$$c(t) = \alpha^* + \frac{(\alpha^*)'}{\beta}\left(1 - e^{-\beta t}\right). \tag{B.22}$$

Appendix C. Proof of Theorem 2

Proof. The expression (10) for the function $g(t)$ can be decomposed as

$$g(t) = \beta e^{-bt}\left[\int_0^{\hat{t}} e^{bs}e^{\frac{2c(s)}{\beta}}ds + \int_{\hat{t}}^t e^{bs}e^{\frac{2c(s)}{\beta}}ds\right] \tag{C.1}$$

for any $\hat{t} \in [0,t]$

Suppose that the function $e^{\frac{2c(s)}{\beta}}$ in Eq. (C.1) in the interval $[\hat{t}, t]$ attains it maximum at t^*. Then

$$g(t) \leq \beta e^{-bt}\left[\int_0^{\hat{t}} e^{bs} e^{\frac{2c(s)}{\beta}} ds + e^{\frac{2c(t^*)}{\beta}} \int_{\hat{t}}^{t} e^{bs} ds\right], \tag{C.2}$$

when t tends to infinity, the previous bound becomes

$$\lim_{t\to\infty} g(t) \leq \frac{\beta}{b} e^{\frac{2\alpha}{\beta}(a_1+a_2)} e^{\frac{2}{\beta}\left(-a_1\alpha e^{-\gamma t^*} + \frac{\alpha\gamma a_1 e^{-\gamma t^*}}{\beta}\left(1-e^{-\beta t^*}\right)\right)} \tag{C.3}$$

Since this bound holds for all $\hat{t}$ and $t^* \geq \hat{t}$, making $\hat{t}$ tend to infinity, it is conclude that

$$\lim_{t\to\infty} g(t) \leq \frac{\beta}{b} e^{\frac{2\alpha}{\beta}(a_1+a_2)} \leq e^{\frac{2\alpha}{\beta}(a_1+a_2)} \tag{C.4}$$

and therefore

$$\lim_{t\to\infty} \int_\Omega |v(\mathbf{x}, t)|^2 dx \leq e^{\frac{2\alpha}{\beta}(a_1+a_2)} \int_\Omega |v_{ob}(\mathbf{x})|^2 dx,$$

References

[1] M.A. Ali, K. Czene, P. Hall, K. Humphreys, Association of microcalcification clusters with short-term invasive breast cancer risk and breast cancer risk factors, Sci. Rep. 9 (1) (2019) 1–8, http://dx.doi.org/10.1038/s41598-019-51186-w, Publisher: Nature Publishing Group.

[2] L. Bertoni, V. Barresi, L.R. Bonetti, S. Caramaschi, A. Mangogna, S. Lionti, P. Azzoni, G. Carnevale, A. Pisciotta, T. Salviato, Poorly differentiated clusters (PDC) in colorectal cancer: Does their localization in tumor matter? Ann. Diagn. Pathol. 41 (2019) 106–111, http://dx.doi.org/10.1016/j.anndiagpath.2019.06.008, Publisher: Elsevier.

[3] M.D. Bora Özveren, L. Türkeri, Vascular endothelial growth factor and thrombospondin-1 mRNA expression in bladder tumors: Correlation with histopathology and prognosis, Bull Urooncol 18 (2019) 18–23, http://dx.doi.org/10.4274/uob.galenos.2018.1179.

[4] L.E.B. Cabrales, A.R. Aguilera, R.P. Jiménez, M.V. Jarque, H.M.C. Ciria, J.B. Reyes, M.A.O. Mateus, F.S. Palencia, M.G. Ávila, Mathematical modeling of tumor growth in mice following low-level direct electric current, Math. Comput. Simulation 78 (1) (2008) 112–120, http://dx.doi.org/10.1016/j.matcom.2007.06.004, Publisher: Elsevier.

[5] L.E.B. Cabrales, J.I. Montijano, M. Schonbek, A.R.S. Castañeda, A viscous modified Gompertz model for the analysis of the kinetics of tumors under electrochemical therapy, Math. Comput. Simulation 151 (2018) 96–110, http://dx.doi.org/10.1016/j.matcom.2018.03.005, Publisher: Elsevier.

[6] L.E.B. Cabrales, J.J.G. Nava, A.R. Aguilera, J.A.G. Joa, H.M.C. Ciria, M.M. González, M.F.n. Salas, M.V. Jarque, T.R. González, M.A.O. Mateus, Modified gompertz equation for electrotherapy murine tumor growth kinetics: Predictions and new hypotheses, BMC Cancer 10 (1) (2010) 1–14, http://dx.doi.org/10.1186/1471-2407-10-589, Publisher: Springer.

[7] E.M. Calzado, J.L.G. Rodríguez, L.E.B. Cabrales, F.M. García, A.R.S. Castañeda, I.M.G. Delgado, L.M. Torres, F.V.G. Uribazo, M.M. González, S.C.A. Brooks, Simulations of the electrostatic field, temperature, and tissue damage generated by multiple electrodes for electrochemical treatment, Appl. Math. Model. 76 (2019) 699–716, http://dx.doi.org/10.1016/j.apm.2019.05.002, Publisher: Elsevier.

[8] E.M. Calzado, H. Schinca, L.E.B. Cabrales, F.M. García, P. Turjanski, N. Olaiz, Impact of permeabilization and pH effects in the electrochemical treatment of tumors: Experiments and simulations, Appl. Math. Model. 74 (2019) 62–72, http://dx.doi.org/10.1016/j.suronc.2009.12.002, Publisher: Elsevier.

[9] A.R.S. Castañeda, E.R. Torres, N.A.V. Goris, M.M. González, J.B. Reyes, V.G.S. González, M. Schonbek, J.I. Montijano, L.E.B. Cabrales, New formulation of the gompertz equation to describe the kinetics of untreated tumors, PLoS One 14 (11) (2019) e0224978, http://dx.doi.org/10.1371/journal.pone.0224978, Publisher: Public Library of Science San Francisco, CA USA.

[10] D.R. Caswell, C. Swanton, The role of tumour heterogeneity and clonal cooperativity in metastasis, immune evasion and clinical outcome, BMC Med. 15 (1) (2017) 1–9, http://dx.doi.org/10.1186/s12916-017-0900-y, Publisher: BioMed Central.

[11] Y. Chen, J.S. Lowengrub, Tumor growth in complex, evolving microenvironmental geometries: A diffuse domain approach, J. Theoret. Biol. 361 (2014) 14–30, http://dx.doi.org/10.1016/j.jtbi.2014.06.024, Publisher: Elsevier.

[12] Y. Chen, J.S. Lowengrub, Tumor growth and calcification in evolving microenvironmental geometries, J. Theoret. Biol. 463 (2019) 138–154, http://dx.doi.org/10.1016/j.jtbi.2018.12.006, Publisher: Elsevier.

[13] H. Ciria, M. Quevedo, L. Cabrales, R. Bruzón, M. Salas, O. Pena, T. González, D. López, J. Flores, Antitumor effectiveness of different amounts of electrical charge in Ehrlich and fibrosarcoma sa-37 tumors, BMC Cancer 4 (1) (2004) 87, http://dx.doi.org/10.1186/1471-2407-4-87.

[14] O. Clatz, M. Sermesant, P.-Y. Bondiau, H. Delingette, S.K. Warfield, G. Malandain, N. Ayache, Realistic simulation of the 3-D growth of brain tumors in MR images coupling diffusion with biomechanical deformation, IEEE Trans. Med. Imaging 24 (10) (2005) 1334–1346, http://dx.doi.org/10.1109/TMI.2005.857217, Publisher: IEEE.

[15] A.D. Conger, M.C. Ziskin, Growth of mammalian multicellular tumor spheroids, Cancer Res. 43 (2) (1983) 556–560, Publisher: AACR.

[16] I. Dagogo-Jack, A.T. Shaw, Tumour heterogeneity and resistance to cancer therapies, Nat. Rev. Clin. Oncol. 15 (2) (2018) 81, http://dx.doi.org/10.1038/nrclinonc.2017.166, Publisher: Nature Publishing Group.

[17] M.G. Di Trani, M. Nezzo, A.S. Caporale, R. De Feo, R. Miano, A. Mauriello, P. Bove, G. Manenti, S. Capuani, Performance of diffusion kurtosis imaging versus diffusion tensor imaging in discriminating between benign tissue, low and high gleason grade prostate cancer, Academic Radiol. 26 (10) (2019) 1328–1337, http://dx.doi.org/10.1016/j.acra.2018.11.015, Publisher: Elsevier.
[18] N. Domínguez-Pinilla, A.M. de Aragón, S.D. Tapias, O. Toldos, J.H. Bernal, M.R. Andrés, L.I. González-Granado, Evaluación de la utilidad del coeficiente de difusión aparente en resonancia magnética para la diferenciación del grado tumoral de los tumores cerebrales pediátricos, Neurología 31 (7) (2016) 459–465, http://dx.doi.org/10.1016/j.nrl.2014.12.003, Publisher: Elsevier.
[19] H. Enderling, M. A.J. Chaplain, Mathematical modeling of tumor growth and treatment, Curr. Pharm. Des. 20 (30) (2014) 4934–4940, URL https://www.ingentaconnect.com/content/ben/cpd/2014/00000020/00000030/art00017, Publisher: Bentham Science Publishers.
[20] K. Esbona, D. Inman, S. Saha, J. Jeffery, P. Schedin, L. Wilke, P. Keely, COX-2 modulates mammary tumor progression in response to collagen density, Breast Cancer Res. 18 (1) (2016) 1–15, http://dx.doi.org/10.1186/s13058-016-0695-3, Publisher: Springer.
[21] M. Esmaeili, A.L. Stensjøen, E.M. Berntsen, O. Solheim, I. Reinertsen, The direction of tumour growth in glioblastoma patients, Sci. Rep. 8 (1) (2018) 1–6, http://dx.doi.org/10.1038/s41598-018-19420-z, Publisher: Nature Publishing Group.
[22] H. von Euler, J.M. Olsson, K. Hultenby, A. Thörne, A.-S. Lagerstedt, Animal models for treatment of unresectable liver tumours: A histopathologic and ultra-structural study of cellular toxic changes after electrochemical treatment in rat and dog liver, Bioelectrochemistry 59 (1–2) (2003) 89–98, http://dx.doi.org/10.1016/S1567-5394(03)00006-9, Publisher: Elsevier.
[23] L.C. Evans, Partial Differential Equations, Vol. 19, American Mathematical Soc., 2010.
[24] J. Fenner, A.C. Stacer, F. Winterroth, T.D. Johnson, K.E. Luker, G.D. Luker, Macroscopic stiffness of breast tumors predicts metastasis, Sci. Rep. 4 (1) (2014) 1–8, http://dx.doi.org/10.1038/srep05512, Publisher: Nature Publishing Group.
[25] L. Ferrante, S. Bompadre, L. Possati, L. Leone, Parameter estimation in a Gompertzian stochastic model for tumor growth, Biometrics 56 (4) (2000) 1076–1081, http://dx.doi.org/10.1111/j.0006-341X.2000.01076.x, Publisher: Wiley Online Library.
[26] K. Foster, H. Schwan, Dielectric permittivity and electrical conductivity of biological materials, in: CRC Handbook of Biological Effects of Electromagnetic Fields, CRC Press, Boca Raton, FL, 1986, pp. 27–99.
[27] R.A. Gatenby, E.T. Gawlinski, A reaction-diffusion model of cancer invasion, Cancer Res. 56 (24) (1996) 5745–5753, URL https://cancerres.aacrjournals.org/content/56/24/5745, Publisher: AACR.
[28] N. Gholizadeh, P.B. Greer, J. Simpson, J. Denham, P. Lau, J. Dowling, H. Hondermarck, S. Ramadan, Characterization of prostate cancer using diffusion tensor imaging: A new perspective, Eur. J. Radiol. 110 (2019) 112–120, http://dx.doi.org/10.1016/j.ejrad.2018.11.026, Publisher: Elsevier.
[29] M.M. González, C.H. Aguilar, F.A.D. Pacheco, L.E.B. Cabrales, J.B. Reyes, J.J.G. Nava, Electrode arrays proposed for electrochemical treatment of tumors: Assessment of their effects on potato pieces [*Solanum tuberosum* L.] as a biological model, Front Oncol. 8 (101) (2018) 1–12.
[30] M.M. González, J.A.G. Joa, L.E.B. Cabrales, A.E.B. Pupo, B. Schneider, S. Kondakci, H.M.C. Ciria, J.B. Reyes, M.V. Jarque, M.A.O. Mateus, Is cancer a pure growth curve or does it follow a kinetics of dynamical structural transformation? BMC Cancer 17 (1) (2017) 1–14, http://dx.doi.org/10.1186/s12885-017-3159-y, Publisher: BioMed Central.
[31] M.M. González, D.F. Morales, L.E. Cabrales, D.J. Pérez, J.I. Montijano, A.R. Castañeda, V.G. González, O.O. Posada, J.A. Martínez, A.G. Delgado, Dose-response study for the highly aggressive and metastatic primary F3II mammary carcinoma under direct current, Bioelectromagnetics 39 (6) (2018) 460–475, http://dx.doi.org/10.1002/bem.22132, Publisher: Wiley Online Library.
[32] N.A.V. Goris, A.R.S. Castañeda, E.E. Ramirez-Torres, J.B. Reyes, L. Randez, L.E.B. Cabrales, J.I. Montijano, Correspondence between formulations of Avrami and Gompertz equations for untreated tumor growth kinetics, Revista Mexicana De Física 66 (5 Sept-Oct) (2020) 632–636, http://dx.doi.org/10.31349/RevMexFis.66.632.
[33] N.A.V. Goris, J.L.G. Rodríguez, M.M. González, B.O. Borges, D.F. Morales, E.M. Calzado, A.R.S. Castañeda, L.M. Torres, J.I. Montijano, V.G.S. González, Efficacy of direct current generated by multiple-electrode arrays on F3II mammary carcinoma: experiment and mathematical modeling, J. Transl. Med. 18 (2020) 1–17, http://dx.doi.org/10.1186/s12967-020-02352-6, Publisher: Springer.
[34] S. Gosling, R. Scott, C. Greenwood, P. Bouzy, J. Nallala, I.D. Lyburn, N. Stone, K. Rogers, Calcification microstructure reflects breast tissue microenvironment, J. Mammary Gland. Biol. Neoplasia 24 (4) (2019) 333–342, http://dx.doi.org/10.1007/s10911-019-09441-3, Publisher: Springer.
[35] R.H. Grantab, I.F. Tannock, Penetration of anticancer drugs through tumour tissue as a function of cellular packing density and interstitial fluid pressure and its modification by bortezomib, BMC Cancer 12 (1) (2012) 1–11, http://dx.doi.org/10.1186/1471-2407-12-214, Publisher: BioMed Central.
[36] G. Gravante, S.L. Ong, M.S. Metcalfe, N. Bhardwaj, G.J. Maddern, D.M. Lloyd, A.R. Dennison, Experimental application of electrolysis in the treatment of liver and pancreatic tumours: Principles, preclinical and clinical observations and future perspectives, Surg. Oncol. 20 (2) (2011) 106–120, http://dx.doi.org/10.1016/j.suronc.2009.12.002, Publisher: Elsevier.
[37] D. Hanahan, R.A. Weinberg, Hallmarks of cancer: The next generation, Cell 144 (5) (2011) 646–674, http://dx.doi.org/10.1016/j.cell.2011.02.013, Publisher: Elsevier.
[38] L. Hathout, V. Patel, P. Wen, A 3-dimensional DTI MRI-based model of GBM growth and response to radiation therapy, Int. J. Oncol. 49 (3) (2016) 1081–1087, http://dx.doi.org/10.3892/ijo.2016.3595, Publisher: Spandidos Publications.
[39] C. Holandino, C.A.A. Teixeira, F.A.G. de Oliveira, G.M. Barbosa, C.M. Siqueira, D.J. Messeder, F.S. de Aguiar, V.F. da Veiga, W. Girard-Dias, K. Miranda, Direct electric current treatment modifies mitochondrial function and lipid body content in the A549 cancer cell line, Bioelectrochemistry 111 (2016) 83–92, http://dx.doi.org/10.1016/j.bioelechem.2016.05.004, Publisher: Elsevier.
[40] T. Jarm, M. Cemazar, F. Steinberg, C. Streffer, G. Sersa, D. Miklavcic, Perturbation of blood flow as a mechanism of anti-tumour action of direct current electrotherapy, Physiol. Meas. 24 (1) (2003) 75, http://dx.doi.org/10.1088/0967-3334/24/1/306, Publisher: IOP Publishing.
[41] T. Jarm, M. Ĉmaẑar, G. Serŝa, D. Miklavĉiĉ, Blood perfusion in a murine fibrosarcoma tumor model after direct current electrotherapy a study with 86Rb extraction technique, Electro- Magnetobiol. 17 (2) (1998) 273–282.

[42] M.V. Jarque, L. Jing-Hong, L.E.B. Cabrales, F.S. Palencia, H.M.C. Camué, S.A. Brooks, M. Fariñas Salas, Primeras experiencias clínicas en Cuba sobre el uso de la electroterapia en cuatro pacientes con tumores sólidos malignos superficiales, Medisan (2007).
[43] A.M. Jarrett, D.A. Hormuth, S.L. Barnes, X. Feng, W. Huang, T.E. Yankeelov, Incorporating drug delivery into an imaging-driven, mechanics-coupled reaction diffusion model for predicting the response of breast cancer to neoadjuvant chemotherapy: Theory and preliminary clinical results, Phys. Med. Biol. 63 (10) (2018) 105015, http://dx.doi.org/10.1088/1361-6560/aac040, Publisher: IOP Publishing.
[44] H. Jayatilaka, F.G. Umanzor, V. Shah, T. Meirson, G. Russo, B. Starich, P. Tyle, J.S. Lee, S. Khatau, H. Gil-Henn, Tumor cell density regulates matrix metalloproteinases for enhanced migration, Oncotarget 9 (66) (2018) 32556, http://dx.doi.org/10.18632/oncotarget.25863, Publisher: Impact Journals, LLC.
[45] A.K. Jonscher, Dielectric relaxation in solids, J. Phys. D: Appl. Phys. 32 (14) (1999) R57–R70, http://dx.doi.org/10.1088/0022-3727/32/14/201.
[46] N. Klein, B. Mercadal, M. Stehling, A. Ivorra, In vitro study on the mechanisms of action of electrolytic electroporation (E2), Bioelectrochemistry 133 (2020) 107482, http://dx.doi.org/10.1016/j.bioelechem.2020.107482, Publisher: Elsevier.
[47] Y. Kuang, J.D. Nagy, S.E. Eikenberry, Introduction to Mathematical Oncology, CRC Press, 2018.
[48] K.-h. Li, Y.-l. Xin, Y.-n. Gu, B.-l. Xu, D.-j. Fan, B.-f. Ni, Effects of direct current on dog liver: Possible mechanisms for tumor electrochemical treatment, Bioelectromagnetics: J. Bioelectromagn. Soc. Soc. Phys. Regul. Biol. Med. Eur. Bioelectromagn. Assoc. 18 (1) (1997) 2–7, http://dx.doi.org/10.1002/(SICI)1521-186X(1997)18:1<2::AID-BEM2>3.0.CO;2-6, Publisher: Wiley Online Library.
[49] M.B. Lodi, G. Muntoni, A. Ruggeri, A. Fanti, G. Montisci, G. Mazzarella, Towards the robust and effective design of hyperthermic devices: Improvement of a patch antenna for the case study of abdominal rhabdomyosarcoma with 3D perfusion, IEEE J. Electromagn. RF Microw. Med. Biol. 5 (3) (2020) 197–205.
[50] T. Løitegård, D.T. Berntzen, E. Thiis-Evensen, The RECIST criteria compared to conventional response evaluation after peptide receptor radionuclide therapy in patients with neuroendocrine neoplasms, Ann. Nucl. Med. 33 (3) (2019) 147–152, Publisher: Springer.
[51] M. Marušić, Z. Bajzer, J.P. Freyer, S. Vuk-Pavlović, Analysis of growth of multicellular tumour spheroids by mathematical models, Cell Prolif. 27 (2) (1994) 73–94, http://dx.doi.org/10.1111/j.1365-2184.1994.tb01407.x, Publisher: Wiley Online Library.
[52] M. Marušić, S. Vuk-Pavlovic, J.P. Freyer, Tumor growth in vivo and as multicellular spheroids compared by mathematical models, Bull. Math. Biol. 56 (4) (1994) 617–631, http://dx.doi.org/10.1007/BF02460714, Publisher: Elsevier.
[53] A.M. McCarthy, W.E. Barlow, E.F. Conant, J.S. Haas, C.I. Li, B.L. Sprague, K. Armstrong, P. Consortium, Breast cancer with a poor prognosis diagnosed after screening mammography with negative results, JAMA Oncol. 4 (7) (2018) 998–1001, http://dx.doi.org/10.1001/jamaoncol.2018.0352, Publisher: American Medical Association.
[54] A. Neri, D. Marrelli, T. Megha, F. Bettarini, D. Tacchini, L. De Franco, F. Roviello, Clinical significance of multifocal and multicentric breast cancers and choice of surgical treatment: A retrospective study on a series of 1158 cases, BMC Surg. 15 (1) (2015) 1–10, http://dx.doi.org/10.1186/1471-2482-15-1.
[55] E.J.R. Oria, L.E.B. Cabrales, J.B. Reyes, Analytical solution of the bioheat equation for thermal response induced by any electrode array in anisotropic tissues with arbitrary shapes containing multiple-tumor nodules, Revista Mexicana De Física 65 (3) (2019) 284–290, http://dx.doi.org/10.31349/revmexfis.65.284, Publisher: Sociedad Mexicana de Física.
[56] K.J. Painter, T. Hillen, Mathematical modelling of glioma growth: The use of diffusion tensor imaging (DTI) data to predict the anisotropic pathways of cancer invasion, J. Theoret. Biol. 323 (2013) 25–39, http://dx.doi.org/10.1016/j.jtbi.2013.01.014, Publisher: Elsevier.
[57] R. Pregla, W. Pascher, et al., The method of lines, in: Numerical Techniques for Microwave and Millimeter Wave Passive Structures, Vol. 1, Wiley, New York, 1989, pp. 381–446.
[58] A.E.B. Pupo, L.E.B. Cabrales, R.P. Jiménez, Electrotherapy on Cancer: experiment and Mathematical Modeling, Citeseer, 2011, http://dx.doi.org/10.5772/25765.
[59] A.E.B. Pupo, M.M. González, L.E.B. Cabrales, J.B. Reyes, E.J.R. Oria, J.J.G. Nava, R.P. Jiménez, F.M. Sánchez, H.M.C. Ciria, J.M.B. Cabrales, 3D current density in tumors and surrounding healthy tissues generated by a system of straight electrode arrays, Math. Comput. Simulation 138 (2017) 49–64, http://dx.doi.org/10.1016/j.matcom.2017.01.004, Publisher: Elsevier.
[60] A. Rizwan, S.K. Paidi, C. Zheng, M. Cheng, I. Barman, K. Glunde, Mapping the genetic basis of breast microcalcifications and their role in metastasis, Sci. Rep. 8 (1) (2018) 1–10, http://dx.doi.org/10.1038/s41598-018-29330-9, Publisher: Nature Publishing Group.
[61] T. Roque, L. Risser, V. Kersemans, S. Smart, D. Allen, P. Kinchesh, S. Gilchrist, A.L. Gomes, J.A. Schnabel, M.A. Chappell, A DCE-MRI driven 3-D reaction-diffusion model of solid tumor growth, IEEE Trans. Med. Imaging 37 (3) (2017) 724–732, http://dx.doi.org/10.1109/TMI.2017.2779811, Publisher: IEEE.
[62] M.B. Sano, M.R. DeWitt, S.D. Teeter, L. Xing, Optimization of a single insertion electrode array for the creation of clinically relevant ablations using high-frequency irreversible electroporation, Comput. Biol. Med. 95 (2018) 107–117, http://dx.doi.org/10.1016/j.compbiomed.2018.02.009, Publisher: Elsevier.
[63] I. Saénz-de Santa-María, L. Celada, M.-D. Chiara, The leader position of mesenchymal cells expressing N-Cadherin in the collective migration of epithelial cancer, Cells 9 (3) (2020) 731, http://dx.doi.org/10.3390/cells9030731, Publisher: Multidisciplinary Digital Publishing Institute.
[64] W.E. Schiesser, The Numerical Method of Lines: Integration of Partial Differential Equations, Elsevier, 2012.
[65] F.C. Schmeel, Variability in Quantitative Diffusion-Weighted MR Imaging (DWI) Across Different Scanners and Imaging Sites: Is There a Potential Consensus that Can Help Reducing the Limits of Expected Bias? Springer, 2019, http://dx.doi.org/10.1007/s00330-018-5866-4.
[66] I. Serša, K. Beravs, N.J. Dodd, S. Zhao, D. Miklavčič, F. Demsar, Electric current density imaging of mice tumors, Magn. Reson. Med. 37 (3) (1997) 404–409, http://dx.doi.org/10.1002/mrm.1910370318, Publisher: Wiley Online Library.

[67] B.P. Sommeijer, L.F. Shampine, J.G. Verwer, RKC: An explicit solver for parabolic PDEs, J. Comput. Appl. Math. 88 (2) (1998) 315–326, http://dx.doi.org/10.1016/S0377-0427(97)00219-7, Publisher: Elsevier.
[68] J.-G. Sun, Eigenvalues of Rayleigh quotient matrices, Numer. Math. 59 (1) (1991) 603–614.
[69] L.N. Tran, M.S. Brown, J.G. Goldin, X. Yan, R.C. Pais, M.F. McNitt-Gray, D. Gjertson, S.R. Rogers, D.R. Aberle, Comparison of treatment response classifications between unidimensional, bidimensional, and volumetric measurements of metastatic lung lesions on chest computed tomography1, Academic Radiol. 11 (12) (2004) 1355–1360, http://dx.doi.org/10.1016/j.acra.2004.09.004, Publisher: Elsevier.
[70] F.-C. Tsai, M.-C. Wang, J.-F. Lo, C.-M. Chou, Y.-L. Lin, Spatiotemporal dynamics of the biological interface between cancer and the microenvironment: A fractal anomalous diffusion model with microenvironment plasticity, Theor. Biol. Med. Model. 9 (1) (2012) 1–13, http://dx.doi.org/10.1186/1742-4682-9-36, Publisher: Springer.
[71] V.G. Vaidya, F.J. Alexandro Jr., Evaluation of some mathematical models for tumor growth, Int. J. Biomed. Comput. 13 (1) (1982) 19–35, http://dx.doi.org/10.1016/0020-7101(82)90048-4, Publisher: Elsevier.
[72] J.P. Walker, M.L. Meyers, A.F. Saltzman, S.L. Hecht, N.G. Cost, The natural history of wilms tumor–A case comparison of two different tumors, Urology 130 (2019) 151–154, http://dx.doi.org/10.1016/j.urology.2019.02.015, Publisher: Elsevier.
[73] S.-M. Wang, Electrotherapy-an old technique for a new use, in: Translational Acupuncture Research, Springer, 2019, pp. 407–419, http://dx.doi.org/10.1007/978-3-030-16089-0_10.
[74] J.P. Ward, J.R. King, Mathematical modelling of drug transport in tumour multicell spheroids and monolayer cultures, Math. Biosci. 181 (2) (2003) 177–207, http://dx.doi.org/10.1016/S0025-5564(02)00148-7, Publisher: Elsevier.
[75] L.-B. Weiswald, D. Bellet, V. Dangles-Marie, Spherical cancer models in tumor biology, Neoplasia 17 (1) (2015) 1–15, http://dx.doi.org/10.1016/j.neo.2014.12.004, Publisher: Elsevier.
[76] Q. Wen, J. Zhu, X. Meng, C. Ma, T. Bai, X. Sun, J. Yu, The value of CBCT-based tumor density and volume variations in prediction of early response to chemoradiation therapy in advanced NSCLC, Sci. Rep. 7 (1) (2017) 1–10, http://dx.doi.org/10.1038/s41598-017-14548-w, Publisher: Nature Publishing Group.
[77] N.S. White, C.R. McDonald, N. Farid, J. Kuperman, D. Karow, N.M. Schenker-Ahmed, H. Bartsch, R. Rakow-Penner, D. Holland, A. Shabaik, et al., Diffusion-weighted imaging in cancer: physical foundations and applications of restriction spectrum imaging, Cancer Res. 74 (17) (2014) 4638–4652.
[78] L. Xin, H. Zhao, W. Zhang, C. Liang, Z. Wang, G. Liu, Electrochemical Therapy of Tumors, bioelectromagnetic Medicine, Marcel Dekker Inc., New York, USA, 2004, http://dx.doi.org/10.3109/9780203021651, ISBN 9780429228575.
[79] M. Zanoni, F. Piccinini, C. Arienti, A. Zamagni, S. Santi, R. Polico, A. Bevilacqua, A. Tesei, 3D tumor spheroid models for in vitro therapeutic screening: a systematic approach to enhance the biological relevance of data obtained, Sci. Rep. 6 (1) (2016) 1–11, http://dx.doi.org/10.1038/srep19103, Publisher: Nature Publishing Group.
[80] M. Zhanlong, S. Haibin, F. Xiangshan, S. Jiacheng, N. Yicheng, Variable solitary fibrous tumor locations: CT and MR imaging features, Medicine 95 (13) (2016) http://dx.doi.org/10.1097/MD.0000000000003031, Publisher: Wolters Kluwer Health.
[81] B.-G. Zhou, C.-S. Wei, S. Zhang, Z. Zhang, Y.-J. Shen, J. Wang, H.-M. Gao, Electrochemotherapy inhibited breast cancer MDA-MB231 cell migration and invasion through PI3k/AKT signal pathway, Int. J. Clin. Exp. Med. 9 (9) (2016) 18513–18518, http://dx.doi.org/10.1055/s-0034-1376977.